
Master Thesis : Experimental Study of Scale Effects of a Multi-Body Floating Solar Photovoltaic Power Plant

Auteur : Mosciatti Urzua, Ezio Antonio

Promoteur(s) : Rigo, Philippe

Faculté : Faculté des Sciences appliquées

Diplôme : Master : ingénieur civil mécanicien, à finalité spécialisée en "Advanced Ship Design"

Année académique : 2023-2024

URI/URL : <http://hdl.handle.net/2268.2/19550>

Avertissement à l'attention des usagers :

Tous les documents placés en accès ouvert sur le site le site MatheO sont protégés par le droit d'auteur. Conformément aux principes énoncés par la "Budapest Open Access Initiative"(BOAI, 2002), l'utilisateur du site peut lire, télécharger, copier, transmettre, imprimer, chercher ou faire un lien vers le texte intégral de ces documents, les disséquer pour les indexer, s'en servir de données pour un logiciel, ou s'en servir à toute autre fin légale (ou prévue par la réglementation relative au droit d'auteur). Toute utilisation du document à des fins commerciales est strictement interdite.

Par ailleurs, l'utilisateur s'engage à respecter les droits moraux de l'auteur, principalement le droit à l'intégrité de l'oeuvre et le droit de paternité et ce dans toute utilisation que l'utilisateur entreprend. Ainsi, à titre d'exemple, lorsqu'il reproduira un document par extrait ou dans son intégralité, l'utilisateur citera de manière complète les sources telles que mentionnées ci-dessus. Toute utilisation non explicitement autorisée ci-avant (telle que par exemple, la modification du document ou son résumé) nécessite l'autorisation préalable et expresse des auteurs ou de leurs ayants droit.



UNIVERSIDAD
POLITÉCNICA
DE MADRID



With the support of the
Erasmus+ Programme
of the European Union

Experimental Study of Scale Effects of a Multi-Body Floating Solar Photovoltaic Power Plant

submitted on December 8, 2023

by

MOSCIATTI URZÚA Ezio Antonio

Av. de la Memoria, 4, Madrid

28040

eziomosciatti@gmail.com

Student ID No.: s217680

Supervisor:

Professor Simone Saettone

Universidad Politécnica de Madrid

First Reviewer:

Professor Pierre Ferrant

1 Rue de la Noë, Nantes

44300

France

Second Reviewer:

Antonio Villalba Herreros, Ph.D.

Av. de la Memoria, 4, Madrid

28040

Spain



MASTER THESIS

[This page is intentionally left blank]

Contents

List of Figures	iv
List of Tables	vi
ABSTRACT	viii
ACKNOWLEDGMENTS	1
1 INTRODUCTION	2
2 RECsolar CONCEPT	3
2.1 Array design	3
2.2 Current setup	4
3 TESTS DEFINITION	6
3.1 Froude similarity	6
3.2 Definition of tests parameters	7
3.2.1 <i>Canal characteristics</i>	7
3.2.2 <i>Scales definition</i>	9
3.2.3 <i>Array definition</i>	11
3.3 Models building	15
3.4 Springs	17
3.4.1 <i>Springs fabrication</i>	18
4 ACQUISITION METHODS	22
4.1 Wave probes	22
4.2 Forces acquisition	23
4.2.1 <i>Load cells</i>	24
4.2.2 <i>Connection of the DAQ</i>	26
4.2.3 <i>LabVIEW</i>	28
4.2.4 <i>Load cell calibration</i>	28
4.3 Motion capture	30
5 MOORING LINES FORCE ANALYSES	32
6 MOTIONS ANALYSES	36
6.1 Single panel decay tests	36
6.2 Array decay tests	39
6.3 Wave tests observations	42
6.4 Motions analyses results	46

6.4.1	General approach	46
6.4.2	Detailed approach	47
7	Conclusions	50
	References	51

List of Figures

1	Towing tank master students team.	1
2	Illustration of complete FPV array. (Jiang, Dai, Saettone, 2023)	4
3	Towing tank experimental setup.	5
4	Final setup of one of the performed tests.	5
5	Wave generator limits for a depth of 2.2 m.	8
6	Waves run for profile checking.	9
7	Time series of free surface elevation for a wave set to $H=254$ mm and $T=1.553$ s.	9
8	Wave similarity.	10
9	Time series of surface elevation for wave.	12
10	Difference in wave height readings between center and side probes.	12
11	Tests waves' characteristics.	14
12	Le Méhauté's diagram.	14
13	FFT of the wave elevation time series for wave 2 d.	15
14	Building process of the smallest model.	16
15	Building process of the biggest model.	17
16	Spring characterization test setup.	19
17	Tested elasticity of springs.	19
18	Wave probes calibration linear regression.	23
19	Load cells setup	24
20	Data acquisition system.	26
21	Welding of a load cell to a RS 232 connector.	27
22	Pin configuration of load cell and DAQ.	27
23	Load cell S2M 832 calibration linear regression.	29
24	Model c with markers.	31
25	Raw versus clean data for line 1, test 1 a.	32
26	Raw versus clean data for line 1, test 1 d.	33
27	Clean time series of line forces for test 1 d	33
28	Parabolic shape of mooring line in 1:60 scale model.	35
29	Execution of a decay test on a single panel.	36
30	Time series of roll decay test.	37
31	Decay tests in heave overview.	37
32	Decay tests in pitch overview.	38
33	Decay tests in roll overview.	38
34	Sway decay tests on array models.	40
35	Surge decay tests on array models.	41
36	Raw time series from wave 4 c.	43

37	Raw vs. filtered time series in surge for test 1c.	43
38	Initial position of markers for wave 2b.	44
39	Sway time series from test b 4 (third repetition).	45
40	Surge time series from test a 1.	45
41	Excursions in surge and sway as a function of the scale, for different wave steepness values.	47
42	Sway average amplitude by row.	48
43	Surge average amplitude by row.	48

List of Tables

1	Froude scale ratios of important variables.	7
2	Final scale ratio values for each model.	11
3	Array dimensions for different configurations.	13
4	Final Array dimensions for all models.	13
5	Wet vs dry characteristics of scaled modules.	15
6	Springs stiffness definition.	18
7	Springs pretension definition.	18
8	Springs characteristics.	20
9	Model's springs assembly.	20
10	Assembled springs measured vs. target stiffness.	21
11	Wave probe calibration results.	22
12	RJ50 connection cables' color code.	27
13	Load cell S2M 832 calibration results.	29
14	Summary of results from line force readings.	34
15	Front vs rear lines difference in tension amplitude.	35
16	Damping ratios by scale and degree of freedom.	39
17	Observations on array decay tests.	42
18	Summary of main results.	46
19	Central vs. lateral results in surge	49

[This page is intentionally left blank]

DECLARATION OF AUTHORSHIP

I, **Ezio Antonio Mosciatti Urzúa** declare that this thesis and the work presented in it are my own and have been generated by me as the result of my own original research.

Where I have consulted the published work of others, this is always clearly attributed.

Where I have quoted from the work of others, the source is always given. With the exception of such quotations, this thesis is entirely my own work.

I have acknowledged all main sources of help.

Where the thesis is based on work done by myself jointly with others, I have made clear exactly what was done by others and what I have contributed myself.

This thesis contains no material that has been submitted previously, in whole or in part, for the award of any other academic degree or diploma.

I cede copyright of the thesis in favour of the *Universidad Politécnica de Madrid*.

Date: December 8, 2023

Signature:

[This page is intentionally left blank]

ABSTRACT

The scope of this thesis is defined within the framework of the "RECSolar" project, a novel design for a floating photovoltaic power plant.

Initial experimental studies were conducted in 2021, in 1 to 60 scale models, to determine the feasibility of the concept in its hydrodynamic behaviour. The scope of the present work is to verify the presence of scale effects in the models. For this purpose, four models of different scales were built.

The design of the models consists of lightweight semisubmersible modules, arranged in an array and connected between them by ropes. The models were built out of polyurethane rectangular cuboids for the experimental campaigns, connected by thin polypropylene strings. The mooring system was a four-point horizontal mooring system.

The tests were performed in the towing tank at the *Canal de Ensayos Hidrodinámicos* of the *Universidad Politécnica de Madrid*. Each model was subjected to five different regular waves, respecting the similarity between the different scales.

The data of the response of each model was retrieved by two means: the forces transmitted to the whole structure were measured by load cells connected to each of the mooring lines. Also, the motions of nearly half of the floats were recorded using the Optitrack motion capture system.

The analysis of these data allowed to reveal the presence of important scale effects between the models, which invalidate the extrapolation of the results to full scale through Froude similarity.

ACKNOWLEDGEMENTS

It is in order to salute the help from the many people who at one point or another were involved in this project with me.

First and foremost, Professor Saettone's involvement not only covering his role as supervisor, but actively working with me to tackle the many problems that arose, whether they were of a technical or practical nature.

Along the same lines, recognition is due to my dear friend Abdulelah Al-Ghuwaidi, who worked side by side with me on this project until the building of the models, without whose support the tight deadlines would probably not have been met.

Finally, I would like to express my gratitude towards the rest of the people who found themselves compelled to help me with one of the many tasks that could not be done by me alone, particularly during the testing campaign, especially to Fernando Pintó, Alejandro Guereño, Gustavo Acosta, Hugo Ferreiro and Anita Guix.



Figure 1: Towing tank master students team.

1 INTRODUCTION

Renewable energy is at the heart of sustainable development, one of the leading contemporary issues. One of the flag goals against this is to limit global warming to 1.5 °C with respect to pre-industrial levels, as set in the Paris Agreement (UNFCCC,2015). To achieve this, Global emissions should drop by 45% by 2030, and to zero by 2050, with respect to 2010 levels (IPCC,2022).

This is linked to the ever-growing global energy demand. According to Conti, Hotltberg et al. (2016) energy demand should experience a growth of 48% between 2012 and 2040. In this context, the energy sector, which represents a fifth of the global final energy consumption shows particular development: the share of renewables in that sector increased from 19.7 percent in 2010 to 26.2 percent in 2019 (UN, 2022).

Within the renewable energy sources, solar is the fastest-growing. Only in Europe, it has gone from about 130 MW to 110 GW of installed capacity in the last twenty years (Nørgaard, Petter, 2019). This technology sees commercial application in different contexts, mainly rooftops and ground-mounted plants, but also on onshore water bodies, mainly reservoirs, on floating structures.

While this last typology of environments shows great potential, with a total surface area available of over 400 000 km² (The World Bank, 2019) and benefits from relatively merciful environmental conditions with low wind, waves, and current loads, when looking at specific regions, it is found that many places could benefit from offshore solutions. In fact, a number of projects and concepts have seen the day during the last decade (Cazzaniga, Rosa-clot, 2021), but only a few of them have a technology readiness level over four.

The RECSolar project was born with the perspective of developing a concept that could endure harsh conditions while tackling the main downside of offshore FPV: its cost. The structure would be conformed by a lattice of soft-connected standardized floating modules, made of lightweight materials.

So far, two rounds of experiments have been performed for these models at the *Canal de Ensayos Hidrodinámicos* of the Universidad Politécnica de Madrid. Both of them focused on the motion performance of simple scale models of the design concept. The first, involving a small 2-by-3 modules model, had the objective of determining the performance under harsh conditions. The second involved a 12-by-18 modules array, i.e. the whole array proposed in the concept design.

The objective of this work was to verify whether or not scale effects would be an issue for such models. In order to do so, first, an assessment of the capabilities of the resources at hand was carried out. With that in mind, the tests were defined, the models designed, and then, the tests were performed. The last two chapters will review the results obtained. The final chapter of this document will contain the conclusions of this work.

2 RECsolar CONCEPT

2.1 Array design

In this section is presented the conceptual evolution of RECsolar, and some considerations for the chosen modules and material. It is important to note that the intricate aspects of the design, such as module geometry and material composition, fall beyond the purview of this chapter, which role is simply to offer an overview of the concept, since it was defined by others than the author.

The RECsolar concept draws inspiration from multiple sources, including the 5-MW coastal FPV project off the coast of Woodlands in Singapore, the interwoven nets commonly seen in Norwegian fish cages, and the cost-effective floating wind turbine design known as TetraSpar (Pereya, Jiang et al. 2018). Diverging from the conventional FPV approach that employs rigid or semi-rigid connections, a RECsolar farm would employ a lattice of flexibly interconnected modules to support PV panels. This unique configuration allows for significantly different dispositions even in the most extreme sea conditions.

Following long technical assessments and extensive round table discussions involving industrial partners and subject matter experts, the foundational design of individual modules and the structure of the connection system were established.

The design principles governing the structural system of Floating Photovoltaic (FPV) systems, conformed by floats acting as support structures for solar panels, and moorings, closely resemble those applied to other offshore structures, as outlined in DNVGL's guidelines (2018).

Additionally, the recommended practice mandates the modeling of extreme environmental conditions and the assessment of global loads and dynamic responses. These environmental loads include factors such as waves, wind, current, ice, and seismic effects. However, due to the nascent stage of the FPV industry, calibrated partial safety factors specific to ultimate, fatigue, and accidental limit states are not yet available for design verification.

The design philosophy of the RECsolar offshore Floating Photovoltaic (FPV) system revolves around three core principles:

- **Minimal Environmental Loads:** The first principle emphasizes the importance of minimizing environmental loads. This approach guides the design towards lightweight float structures and employs a distinctive, flexible connection system utilizing ropes.
- **Low Cost:** The second principle dictates that RECsolar components adhere to a straightforward and economical configuration. This design philosophy ensures that the components can be produced, transported, assembled, installed, maintained, and repaired at minimal expense.

These fundamental principles of the RECsolar FPV system, aim to strike a harmonious balance between environmental considerations, cost-efficiency, and sustainability.

Figure 2 illustrates a RECsolar farm featuring all crucial components, including FPV arrays, floating linkages, a floating transformer, connections, and mooring systems. Each FPV array possesses a power generation capacity of 1 MW, and is constructed from multiple standard floats, interconnected using ropes to address fatigue concerns. The floats were designed with a low freeboard to minimize wind loads and enhance cooling efficiency, thanks to the proximity of the panels to the water surface.

Each float is comprised of a porous pontoon and six cylindrical floats. The porous pontoon is strategically designed with vertical cut-outs to bolster out-of-plane flexural rigidity and facilitate improved air circulation between the solar panels and the water surface.

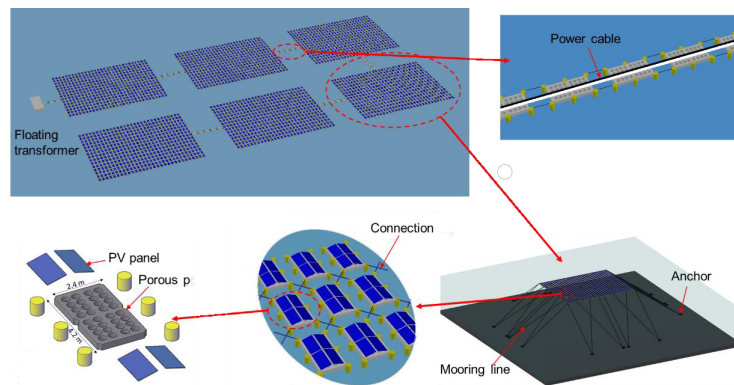


Figure 2: Illustration of complete FPV array. (Jiang, Dai, Saettone, 2023)

2.2 Current setup

The current setup's particular details will be discussed in detail in the following chapters. For now, a simple overview of the setup will be given.

In the model test, the geometrical similarity, kinematic similarity, and dynamic similarity need to be satisfied. If the Froude scaling is followed, the ratio of the inertial and gravitational forces will be the same between the full- and model-scale structures.

Figure 3 shows a schematic view of the setup implemented for the experimental campaign. A four-point above-water-level mooring system was employed to secure the model, ensuring it remained stationary without influencing the wave motion responses. It's important to note that this restrained system does not represent a practical mooring method, but is frequently used to assess the loading and response of floating offshore platforms when catenary mooring lines are absent, as is the case here.

The models would be made of a series of panels as shown in the image, from here on after called modules. The modules would be cross-linked with soft ropes.

The mooring lines, departing from each corner of the array, would be linked to load cells in order to register the force exerted on the rope.

Some of the modules would be equipped with a reflecting marker, thanks to which it would become possible to register the motions of a single module.

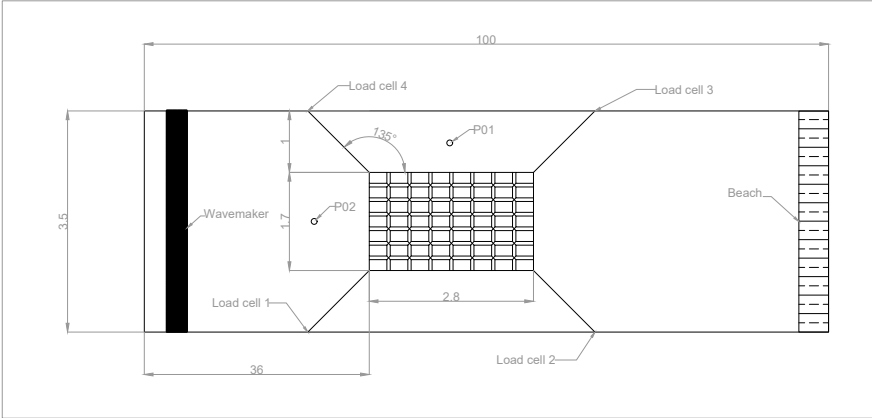


Figure 3: Towing tank experimental setup.

Figure 4 shows the finalized setup for one of the tests performed during this work.

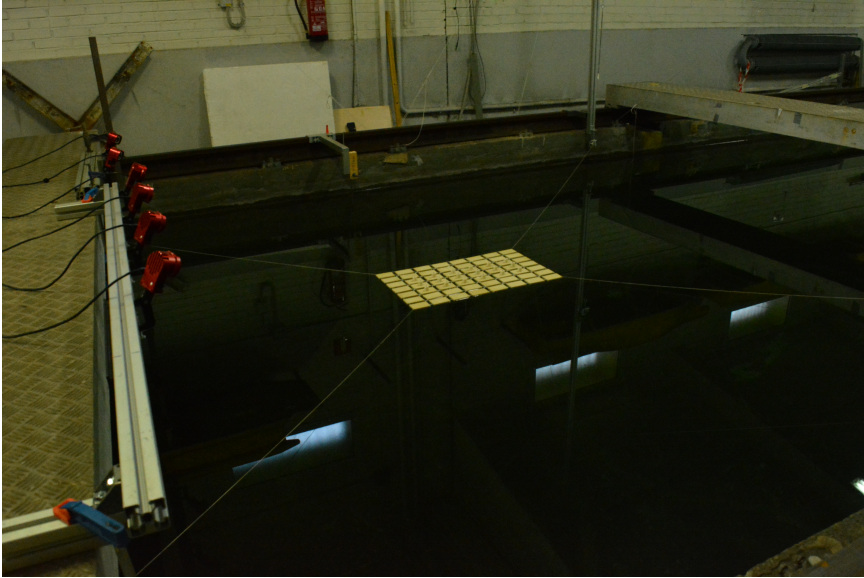


Figure 4: Final setup of one of the performed tests.

3 TESTS DEFINITION

This chapter shows the different steps taken in preparation for the experimental campaign. To do so, firstly, the theory behind Froude similarity will be briefly described. Then, in Chapter 3.2 are reviewed the capabilities of the infrastructure in which the experiments were performed. This will turn out to be the defining parameter when deciding what tests to perform.

Later on, the process of building the model will be briefly depicted.

3.1 Froude similarity

Froude similarity is a concept used to predict the behavior of full-scale models based on that of model-scale prototypes. The working principle of this concept is to keep constant the ratio of inertial forces to gravitational forces in a fluid flow (Froude, 1879). This ratio is called the *Froude number*, and is defined as follows:

$$F_r = \frac{V}{\sqrt{g * L}} \quad (1)$$

Where:

- V is the velocity of the fluid (or the model) relative to the reference frame.
- g is the gravitational acceleration.
- L is a characteristic length, such as the length of the model.

Froude similarity assumes that the Reynolds number stays constant between the scales. However, in certain cases, as flow velocities change due to geometric scaling, the Reynolds number might fall into different flow regimes.

On top of this, viscous effects are not accounted for. Viscous forces might play a more significant role in the smaller-scale model due to higher surface area-to-volume ratios, leading to deviations from the predicted behavior.

In the case of these studies, the model array is relatively lightweight compared with traditional offshore structures. This makes the loads of the array inertia-dominated, and the viscous drag is expected to play a much less important role, even in extreme sea states. The following Table 1 synthesizes the scaling factor for different variables, according to the Froude similarity principle.

Table 1: Froude scale ratios of important variables.

Parameter	Dimension	Froude scale ratio
Linear dimensions	L	λ_s
Area	L^2	λ_s^2
Volume	L^3	λ_s^3
Rotation	-	-
Time	T	$\lambda_s^{\frac{1}{2}}$
Velocity	L/T	$\lambda_s^{\frac{1}{2}}$
Acceleration	L/T^2	-
Mass	M	λ_s^3
Force	MLT^{-2}	λ_s^3

3.2 Definition of tests parameters

As previously stated, tests on different regular wave conditions were to be performed on models of different scales. The smallest scale was set to 1:60 the same as that of the experiments of the 2021 campaigns. The number of models and the wave characteristics were defined in function of the limitations of the facilities.

3.2.1 Canal characteristics

The canal is 100 *m* long, 3.8 *m* wide, and 2.2 *m* deep. At one end, a beach extends for 8.8 *m*. In the opposite end, a single flap wave generator can make waves of up to 0.30 *m* in height, and of periods as short as 0.7 *s*.

Figure 5 shows, in blue, the limits of the wave generator. As can be seen, the limits are formed by three curves. The curve on the left is defined by the maximum acceleration the piston can withstand. The horizontal section represents spilling over the edge of the basin of the canal. Finally, the curve on the right is set by the maximum stroke of the piston.

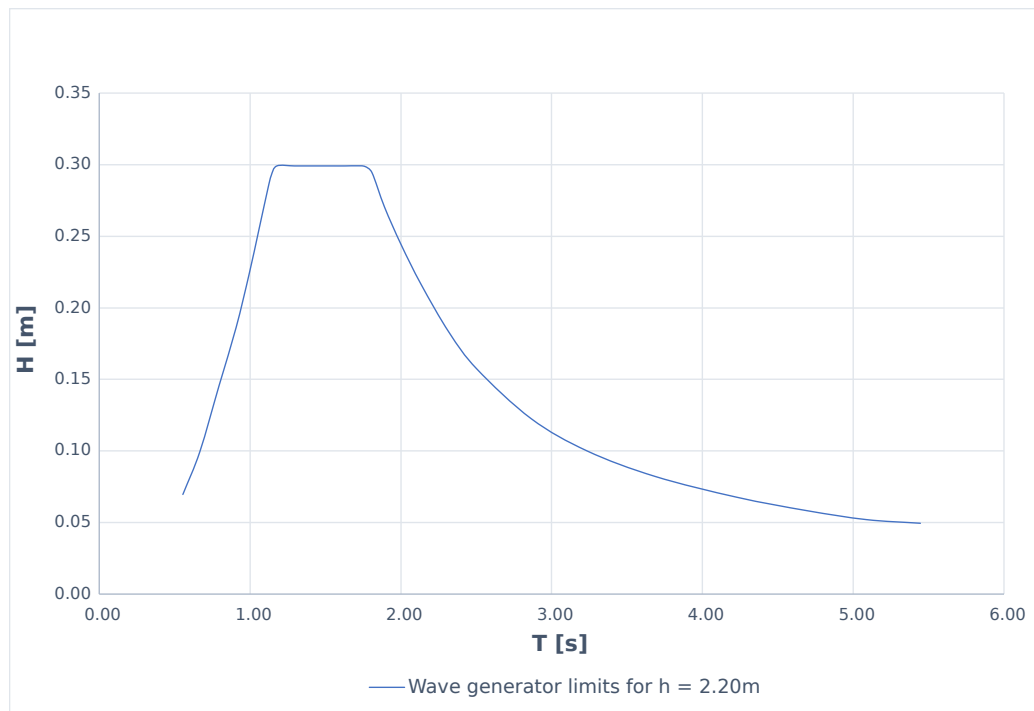


Figure 5: Wave generator limits for a depth of 2.2 m.

Nevertheless, in a more practical sense, it was necessary to stay under 4% of steepness of the waves to ensure a proper wave profile.

Around this time, a few waves were run with pedagogic goals. It was necessary for the author to understand things such as the calibration of the wave probes, the handling of the wave generator program, the connection of the acquisition systems, the usage of the carriage control panel, etc.

During these trials, though, it was observed that for relatively high waves, the profile seemed to lose its proper shape. Figure 6 shows as orange dots the different waves checked. Figure 7 shows the time series resulting from one of these tests.

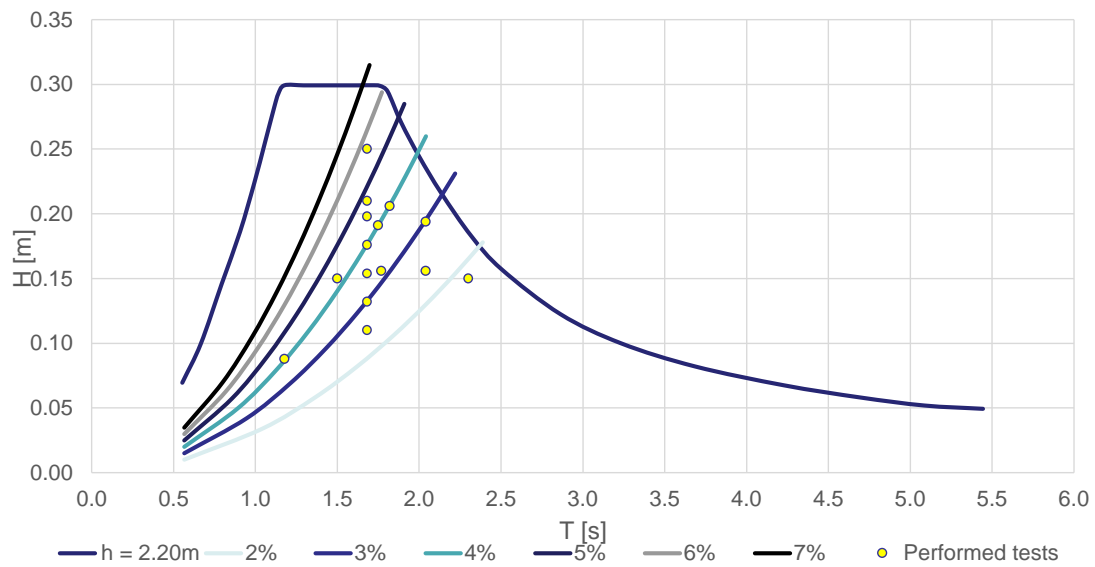


Figure 6: Waves run for profile checking.

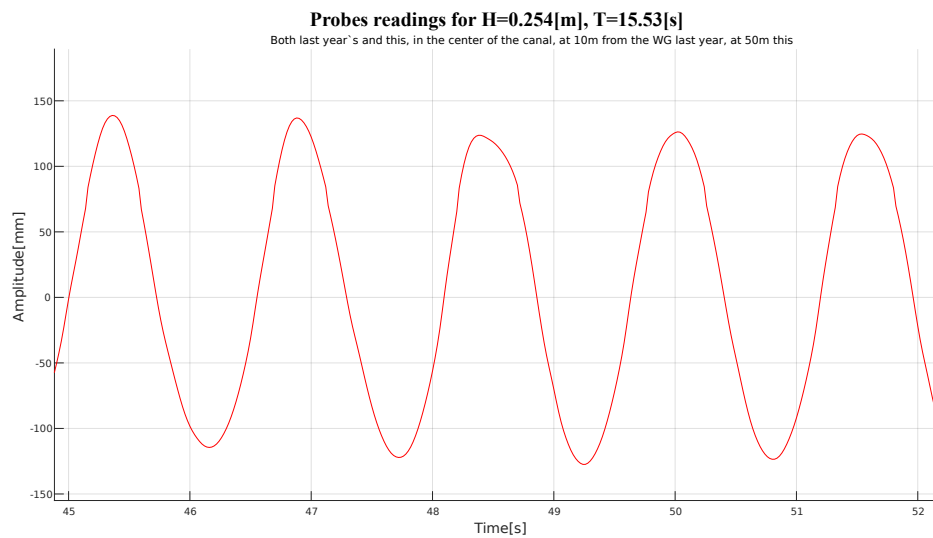


Figure 7: Time series of free surface elevation for a wave set to $H=254\text{ mm}$ and $T=1.553\text{ s}$.

After this, it was concluded that in order to avoid encountering this kind of problem, it was better to limit the wave height to 16 cm .

3.2.2 Scales definition

While the strict minimum to define the presence of scale effects is three different scales, it was considered better to make four different ones, so that the trend, if any, would be clearer.

While the smallest model's scale was set, the biggest's was still to be defined. Since, as

explained before, the biggest wave that could be run confidently was about 16 *cm* in height, this would be the limiting factor when deciding the smallest scale.

Taking into consideration the other experimental campaigns performed, it was preferred not to run waves smaller than 2.5 *m* in height, at full scale. Therefore, the smallest allowable scale, from these parameters, was $\lambda_{min} = 2.5/0.16 = 16.6$, which represented an upper, indicative limit for the biggest model.

In order to maximize the range of the scales, rather than testing each model for waves of different heights, it was decided to vary the steepness. Since the steepness is defined as the wave height divided by the wave length, according to the Froude similarity criteria, two waves which have the same steepness are also similar. Figure 8 shows curves for waves of different steepness, in the context of the limits of the wave generator.

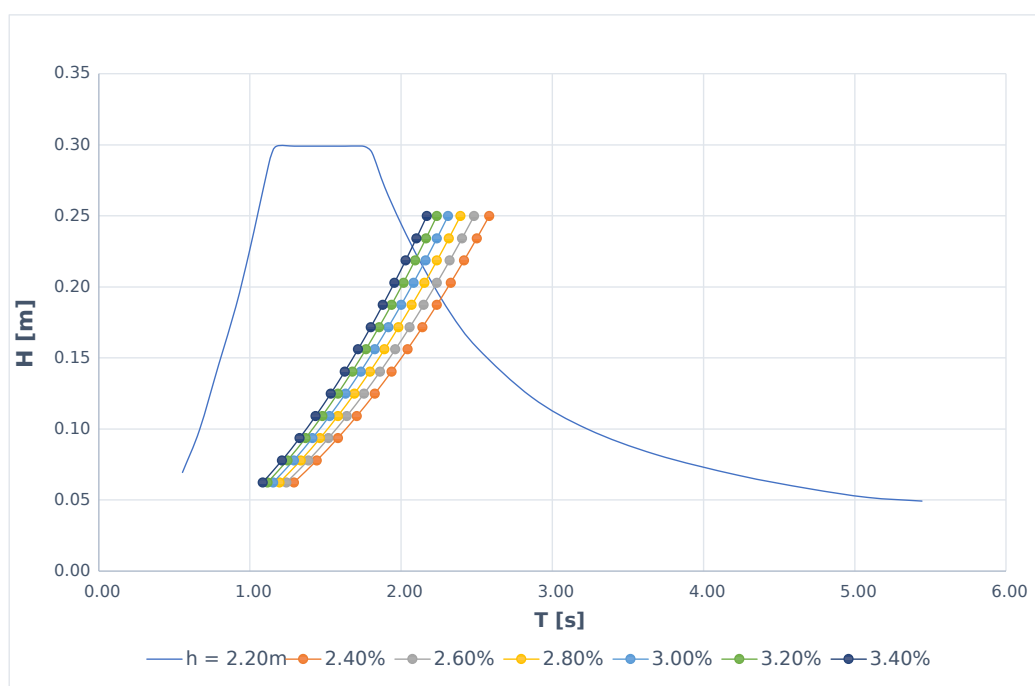


Figure 8: Wave similarity.

Since the steepness range was not extremely large for 16 *cm* waves, it was decided to test only four waves per model, all of them of the same height, and steepness ranging from 2.4% to 3.3%, in steps of 0.3%. It was also decided, at this stage, in order to keep nicely rounded ratios between the different scales, to set the biggest scale to 1:16. The other two scales were defined as follows:

- $\lambda_d^{-1} = 16, \quad 60/16 = 3.75$
- $\lambda_c^{-1} = 24, \quad 60/24 = 2.50$
- $\lambda_b^{-1} = 48, \quad 60/48 = 1.25$
- $\lambda_a^{-1} = 60, \quad 60/60 = 1$

Nevertheless, these values were not definitive. Due to practical considerations during construction, which will be discussed in Chapter 3.3, these values were slightly modified:

Table 2: Final scale ratio values for each model.

λ_a^{-1}	λ_b^{-1}	λ_c^{-1}	λ_d^{-1}
60	43.8	23.5	15.5

- $\lambda_d = 15.5$
- $\lambda_c = 23.5$
- $\lambda_b = 43.8$
- $\lambda_a = 60$

3.2.3 Array definition

Until this point, the dimensions of the array were still to be set.

As explained in the introduction, the entire array concept designed is made up of 18x12 modules. Although there was no imperative need to replicate the entire configuration, it was considered interesting to maximize the size of our model arrays to better understand their dynamic performance.

At this juncture, the largest feasible scale had nearly been defined. One further consideration to take into account was that the dimensions of the array were constrained by the width of the canal, so as to avoid potential issues related to wall effects.

To gain a more comprehensive understanding of the influence that wall effects could have on the tests, a series of experiments involving waves with identical characteristics were conducted. The wave chosen was close to the the limit that had been set previously about amplitude and period. Its characteristics follow:

- Wave height $H = 15.6 \text{ cm}$
- Wave period $T = 1.83 \text{ s}$

For these tests, two wave probes were placed in the same transverse plane, 32 m away from the wave generator, the equivalent of 6 wavelengths, so that the waves would be fully developed. The probes were placed in the same transverse plane, one at the center, and the other increasingly close to the wall.

Five waves were run in this configuration. Figure 9 shows the time series of one of them. It is to be noted that, for these tests, the waves were not calibrated, meaning that the wave obtained in the specific point of interest does not necessarily agree with the values imputed into the wave generator controller program, which corresponds to the "target" line.

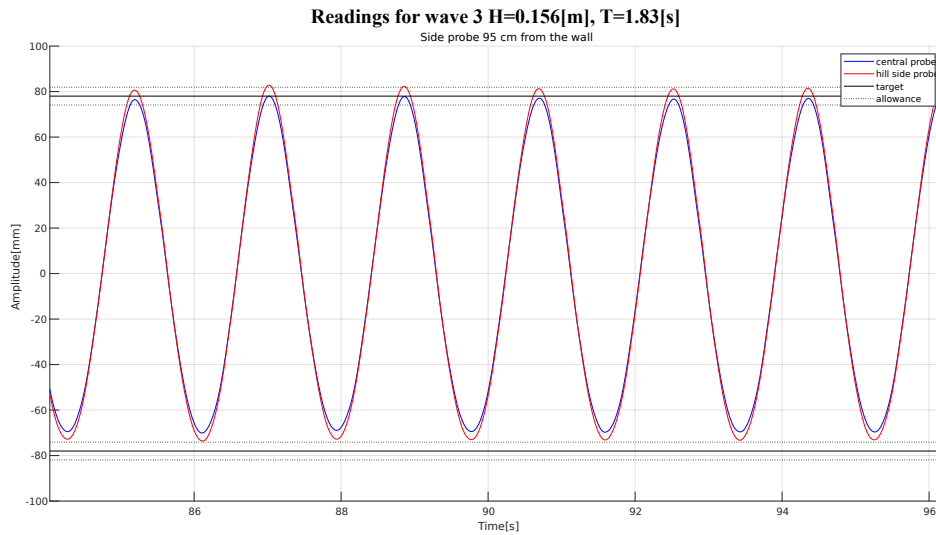


Figure 9: Time series of surface elevation for wave.

Figure 10 shows the resulting average wave height difference between the reading of the central wave probe and that of the side probe for each test, as a function of the distance between them.

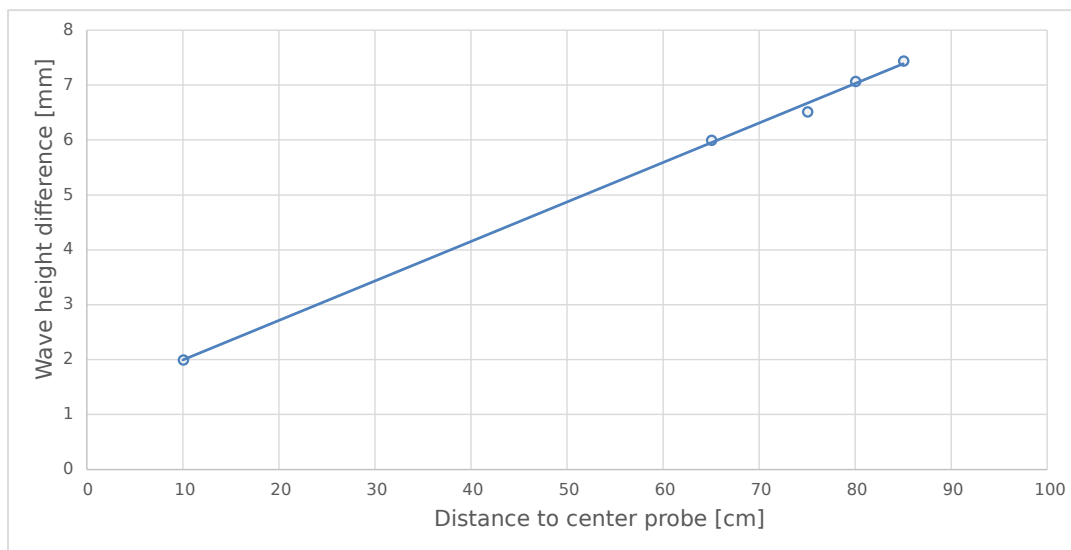


Figure 10: Difference in wave height readings between center and side probes.

From these results, it was found out that in order to stay within a $\pm 5\%$ range from the target wave height, it is better to stay at least one meter away from the walls.

On top of this, it was also preferred to have an odd number of modules in the transverse direction. Table 3 shows the width of the biggest model, in function of the number of modules in the array in the transverse direction.

Table 3: Array dimensions for different configurations.

Scale	1:1	1:15.5		
Module length [m]	4.7	0.303		
Module width [m]	2.9	0.187		
Module height [m]	0.6	0.039		
Space between modules [m]	1	0.065		
Number of transverse modules [-]	3	5	7	9
Array width [m]	0.690	1.194	1.697	2.200
Distance to walls [m]	1.555	1.303	1.052	0.800

The optimum amount of transverse modules was then defined to be seven.

The number of longitudinal modules, instead, was defined in a more subjective approach. The array should not be excessively oblong, so that it still resembles the complete full-scale array configuration, nor too big, so that construction times do not dilate excessively. It was decided to make it 8 modules in length. Table 4 summarizes the final dimensions of the different arrays.

Table 4: Final Array dimensions for all models.

Scale	1:1	1:15.5	1:23.5	1:43.8	1:60
Module length [m]	4.7	0.303	0.200	0.107	0.078
Module width [m]	2.9	0.187	0.123	0.066	0.048
Module height [m]	0.6	0.039	0.026	0.0137	0.010
Space between modules [m]	1	0.065	0.043	0.023	0.017
Array length [m]	44.6	2.887	1.898	1.018	0.743
Array width [m]	26.3	1.679	1.119	0.600	0.438
Distance to walls [m]	-	1.052	1.340	1.600	1.681

Likewise, the final wave characteristics of the waves to perform the tests with, are listed in Table 20 in Appendix B, and represented in Figure 11. In order to lighten the descriptions, from here on further, the waves used to conduct the experiments will be designated by a letter, a through d, that corresponds to the scale, 1:60 through 1:15.5, respectively; and a number, 1 through 4, corresponding respectively to increasing steepness. Again, the table in the Appendix shows all of this in detail.

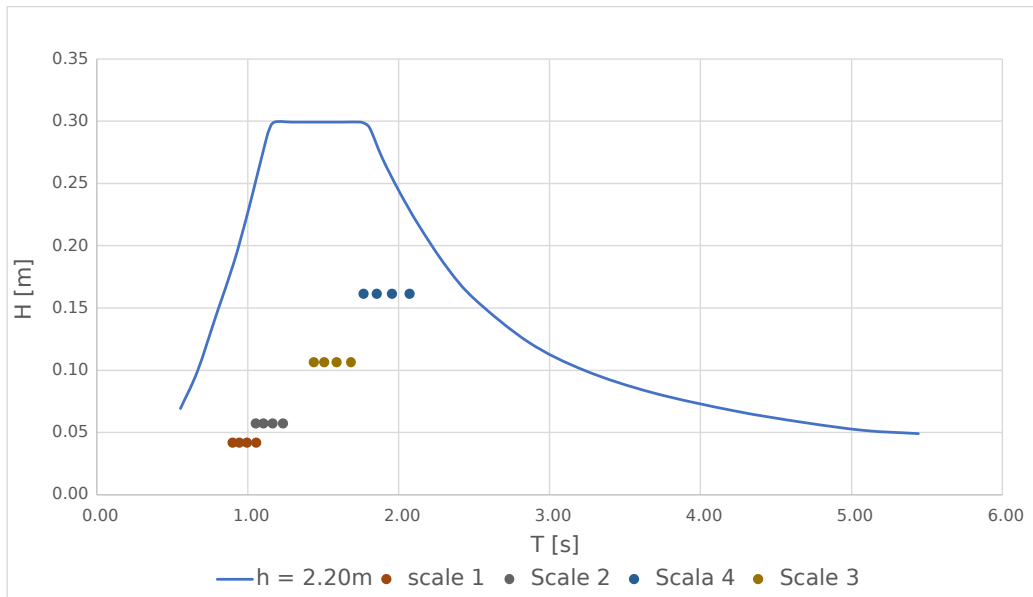


Figure 11: Tests waves' characteristics.

The final two columns in the table provided in the Appendix reveal that the waves employed in these experiments do not conform to linear (Airy's) theory, exhibiting a second-order component instead. Moreover, it's worth noting that the four waves used for the largest model do not conform to the characteristics of deep water waves; they surpass the limit delineated by Le Méhauté's (1969) diagram, depicted in Figure 12. Nevertheless, the second order component is not very pronounced. Figure 13 shows the Fourier transform of the readings of a wave probe during the wave calibration process. The peak corresponding to the second harmonic is clearly visible, but quite insignificant.

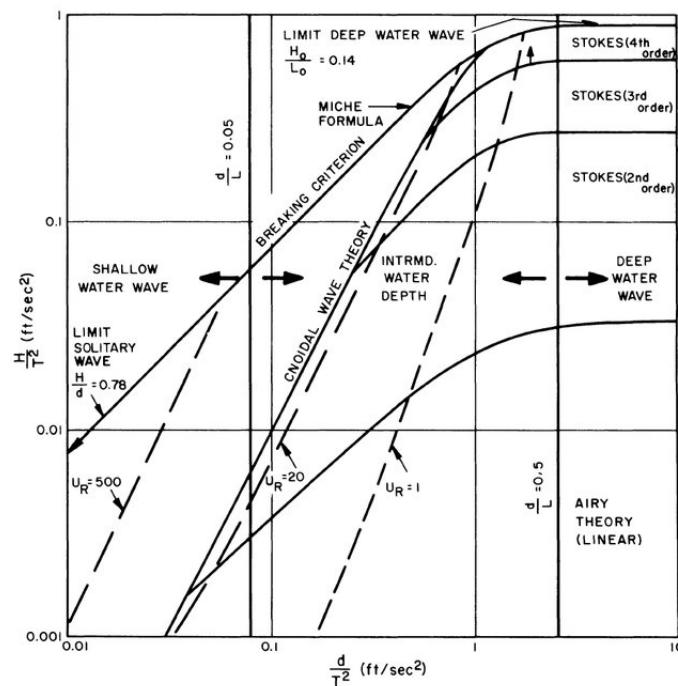


Figure 12: Le Méhauté's diagram.

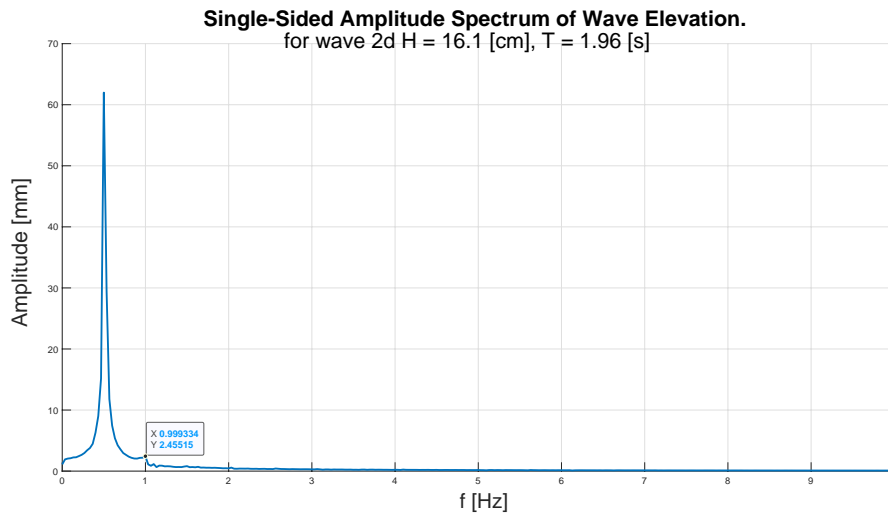


Figure 13: FFT of the wave elevation time series for wave 2 d.

3.3 Models building

As previously explained, the models comprised two components: the modules and the soft connectors. Staying in line with previous experiments, the modules were built out of polyurethane panels with homogeneous mass distribution. This material absorbs a small amount of water over time, resulting in some uncertainties in the experimental results. Table 5 shows the dry and wet density of the modules for each scale. The soft connections were made out of 1.5 mm braided polypropylene rope, of 0.5 g/m of density.

Table 5: Wet vs dry characteristics of scaled modules.

Scale	1:15.5	1:23.5	1:43.8	1:60
Volume [cm^3]	37.9	97.3	630.1	2196.1
Dry weight [g]	11.9	31.6	201.3	689.8
Wet weight [g]	12.9	32.9	207.5	704.9
Dry density [kg/m^3]	314.3	324.7	319.4	314.1
Wet density [kg/m^3]	340.7	338.0	329.3	321.0

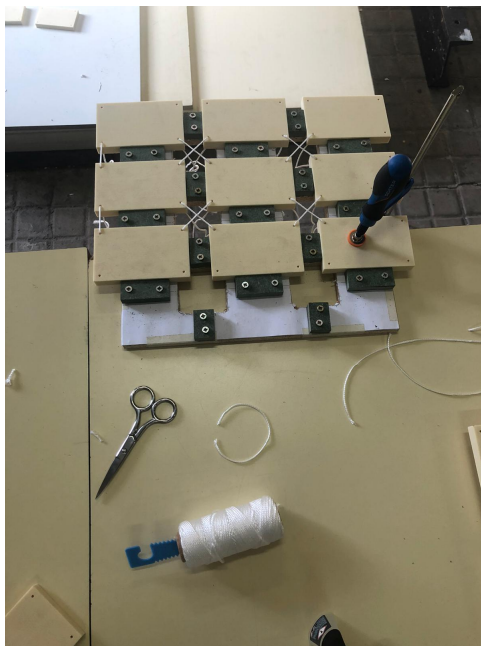
The polyurethane was purchased from *Kingspan* in custom-width 2-by-1 meter panels. However, upon receiving the material, it was observed that the panels' width did not respect the accurate tolerances advertised. To stay in line with the busy schedule of the towing tank, which is typically fully booked, it was decided to adjust the scales to match the received material's width. This approach was favored over the alternative of returning the panels and enduring weeks of waiting for replacements with a higher tolerance, as discussed in Chapter 3.2.2.

This implied not only adapting the scales but also to infringe slightly the boundaries previously set. As all the panels were slightly thicker than expected, the biggest model became even bigger, meaning that its edges would be even closer to the walls and that the

biggest waves would be over 16 *cm* high. Thankfully, upon review of the readings of the wave probes, this did not pose a problem.

Before sending the panels to the in-house carpentry shop to be cut to the specific dimensions of the modules, it was also checked that the new, larger modules, could all be taken from the number of panels bought of each thickness. Although for the biggest model the new dimensions left only four spare modules, the process continued. The carpentry managed to avoid scrapes, and presented the modules cut with an outstanding precision of ± 0.5 *mm*. The models' corners were drilled in order to create a hole through which thread the rope that would become the soft link between the panels. These holes, like the rope itself, were scaled in terms of its position, but not of its dimensions. They were always 2.5 *mm* in diameter.

In order to create the links, the frames shown in Figure 14 were built. In them, the modules would fit tightly, then, the rope would be threaded through the corresponding holes and glued with a medium viscosity cyanoacrylate-based glue, which penetrated and sealed properly the holes with the rope. The leftover rope, that protruded from the bottom of the modules, was cut and filed, so that the base of the modules would regain its flatness.



(a) First step of the array's assembly.



(b) Second step of the array's assembly.

Figure 14: Building process of the smallest model.



(a) First step of the array's assembly.



(b) Second step of the array's assembly

Figure 15: Building process of the biggest model.

3.4 Springs

The rope used for the mooring line is nearly inextensible. To represent the elasticity of a realistic mooring line, a spring links the line and the load cell. In this section is discussed the selection of the main parameters of the springs used for each model. Later, their tweaking will be discussed.

Two parameters about the springs must be defined in the context of these experiments:

- The stiffness k of the springs to be used for each model.
- The pre-tension, P_p load to set for each of them.

The stiffness of the springs should maintain similarity between the models. Going back to Table 1, the Froude scale ratio for the stiffness is λ^2 .

Preferably, the models' natural frequency would not coincide with the frequency of any of the tested waves. Since it is not possible to calculate it analytically, the frequency considered will be that of a simple harmonic oscillator of stiffness equal to $4k$ (the four springs in parallel) and mass equal to that of the whole array. The natural period considered for each model was then calculated as follows:

$$T_n = \frac{2\pi}{\sqrt{\frac{4k}{m}}} \quad (2)$$

At the beginning, it was thought to make the system stiff, so that its natural period would be shorter than the shortest wave. Unfortunately, this would have meant, for the bigger models, using very stiff springs. It was decided, instead, to go in the opposite direction. Since our provider, *La Casa de los Muelles*, had a rather limited stock of springs for these ranges, the main driver for the choice of the final value was the feasibility of obtaining those specific stiffness combining or shortening the springs at our disposal. The target was then set to 4.5 kN/m in full scale. Table 6 shows the main parameters for these

calculations for each scale. The subindex "M" stands for those values referring to model scales, while the subindex "F" stands for those corresponding to full-scale parameters.

Table 6: Springs stiffness definition.

Scale factor	-	1:60	1:43.8	1:23.5	1:15.5
Individual panel weight	[g]	11.9	30.7	198.5	691.8
Array weight	[kg]	0.67	1.72	11.2	38.74
k_F	[kN/m]	4.5	4.5	4.5	4.5
k_M	[N/m]	1.25	2.35	8.15	18.73
$T_{n,M}$	[s]	2.30	2.69	3.67	4.52
Closest wave period	[s]	1.05	1.23	1.68	2.07
Periods ratio	[-]	0.46	0.46	0.46	0.46

Once the stiffness of the springs was decided, the pretension was selected. In the previous campaign, it was set to the equivalent of 50 kN in full scale. It was observed that it would be advantageous to increase it. Nevertheless, the main limitation of this factor was the elongation of the springs, wince the springs were going to be quite soft: in two and a half meters had to fit the load cell, the springs' base length, and their extension under both the pretension and wave loads. It was therefore decided to keep it at the equivalent of 60 kN in full scale. Table 7 shows the parameters related to the pretension for each model.

Table 7: Springs pretension definition.

Scale factor	$P_{p,F}$	$P_{p,M}$	k_m	Spring elongation
[-]	[kN]	[N]	[N/m]	[mm]
1:60	60	0.028	1.25	222
1:43.8	60	0.71	2.35	304
1:23.5	60	4.62	8.15	567
1:15.5	60	16.11	18.73	860

3.4.1 Springs fabrication

To attain springs of the stiffness defined in Table 6, the following were bought:

- Type 1: 20, very soft, 55 mm long, dark springs.
- Type 2: 20, rather soft, 55 mm long, silver springs.
- Type 3: 4, rather stiff, 1 m long, silver springs.

Since no proper denomination of for the different varieties of springs was used at the store, and there were only three different varieties, they were simply called type 1, 2 or 3.

Upon their purchase, the different springs were tested to determine their stiffness. The stiffness of a spring is supposed to vary linearly with the number of spirals it has, or, what

comes to be the same, its length. Nevertheless, springs with too few spirals deviate from this trend. In the same way, connecting many springs may result in a contribution from the death spirals used to connect them. Also, for relatively small loads, the springs can simply not deform (Bongiovanni, Roccati, 1994). Therefore, for types 1 and 2, connections in series were tested, and two others of each were sacrificed: one to check the maximum allowable load, and one that was cut to check for linearity problems because of the low number of spirals..

The tests were performed by attaching one end of the spring to a load cell, and the other to a calibrated weight that was made to oscillate up and down, creating a simple harmonic oscillator. The acquisition method used was very similar to that described in Chapter 4.2. Figure 16 shows the setup of one of these experiments.

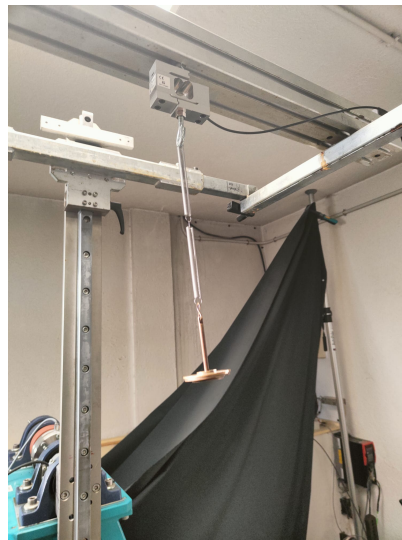
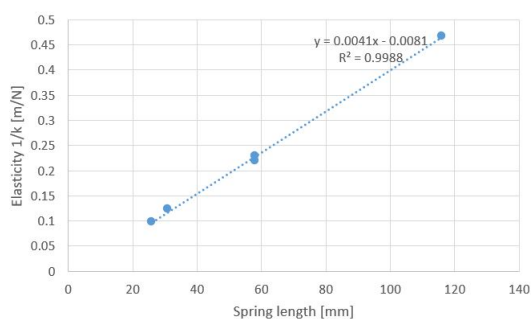
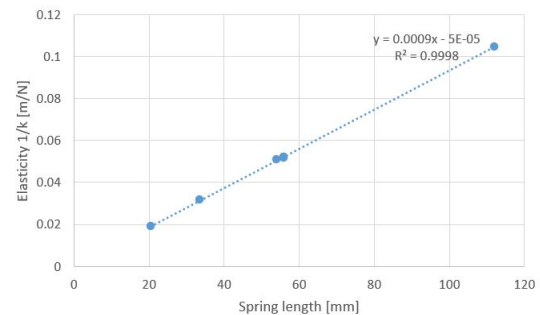


Figure 16: Spring characterization test setup.

A Matlab script, displayed in Appendix C1, was used to extract the stiffness from each test. A low-pass filter was used to smooth out the noise. Figure 17 shows the results found from these tests. The linearity of the springs is easy to observe.



(a) Elasticity of type 1 springs.



(b) Elasticity of type 2 springs.

Figure 17: Tested elasticity of springs.

Type 3 springs, instead, were tested individually, without cutting them, so one such a

trend was not found. Consistent results were found. Table 8 summarizes these findings, with a focus on the length-dependent (L) elasticity $1/k/L$.

Table 8: Springs characteristics.

Spring type	Average $1/k/L$	Available length	Maximum load	Minimum load
[-]	[1/N]	[mm]	[g]	[g]
1	3.90E-3	1100	250	-
2	9.3E-4	1045	750	-
3	2.09E-4	4000	-	100

Table 9 shows how the springs for each model can be created by combining or dividing the available springs (no two different types of springs were connected together).

Table 9: Model's springs assembly.

Scale	Spring type	Target k	required length
[-]	[-]	[N/m]	[mm]
1:60	1	1.25	205
1:43.8	2	2.35	457
1:23.5	3	8.15	587
1:15.5	4	18.73	255

After cutting and assembling the springs, all sixteen of them were checked once again, with a weight relatively close to the pretension for the corresponding model. Table 10 shows the results of these tests.

Once all the assembled springs were within a $\pm 5\%$ of their respective target, they were deemed acceptable.

Table 10: Assembled springs measured vs. target stiffness.

Scale	Test	Mass	Target k	Measured k	error
[-]	[-]	[kg]	[N/m]	[N/m]	[-]
1:60	a1	0.05	1.25	1.24	-0.5%
1:60	a2	0.05	1.25	1.24	-1.0%
1:60	a3	0.05	1.25	1.22	-2.8%
1:60	a4	0.05	1.25	1.25	0.0%
1:43.8	b1	0.25	2.35	2.26	-3.6%
1:43.8	b2	0.25	2.35	2.31	-1.2%
1:43.8	b3	0.25	2.35	2.30	-1.8%
1:43.8	b4	0.25	2.35	2.31	-1.3%
1:23.5	c1	0.5	8.15	8.43	3.5%
1:23.5	c2	0.5	8.15	8.44	3.6%
1:23.5	c3	0.5	8.15	8.27	1.6%
1:23.5	c4	0.5	8.15	8.24	1.1%
1:15.5	d1	1.65	18.73	18.67	-0.3%
1:15.5	d2	1.65	18.73	18.13	-3.2%
1:15.5	d3	1.65	18.73	18.81	0.4%
1:15.5	d4	1.65	18.73	19.04	1.6%

4 ACQUISITION METHODS

In this chapter, we will review the implementation of the systems through which data was collected.

4.1 Wave probes

Resistance wave probes were used throughout this campaign to monitor wave elevation in every test made. These gauges operate by measuring the resistance of the water between a pair of parallel rods. The resistance between the rods is proportional to the immersion depth.

It is important to calibrate them before starting a new set of tests, as they can be affected by various environmental factors, such as the water temperature. This is done by submerging the probe to different depths and recording the tension registered for each of them. Then, the results are linearized through linear regression. Table 11 shows the consecutive depths to which the probe was submerged, and one example of results found for probes P01 and P02. Figure 18 shows the same results plotted, and their trend line. From the r squared value of the trend lines, we can see that the accuracy was excellent for almost twice the range we are interested in.

Table 11: Wave probe calibration results.

Depth [mm]	P 02 [V]	P 01 [V]
0	0.98	1.65
150	8.18	9.29
100	5.75	6.72
50	3.35	4.16
0	0.92	1.58
-50	-1.5	-0.99
-100	-3.90	-3.53
-150	-6.26	-6.01
-100	-3.91	-3.54
-50	-1.54	-1.04
0	0.89	1.55
50	3.30	4.11
100	5.70	6.67
150	8.09	9.19
-150	-6.28	-6.03

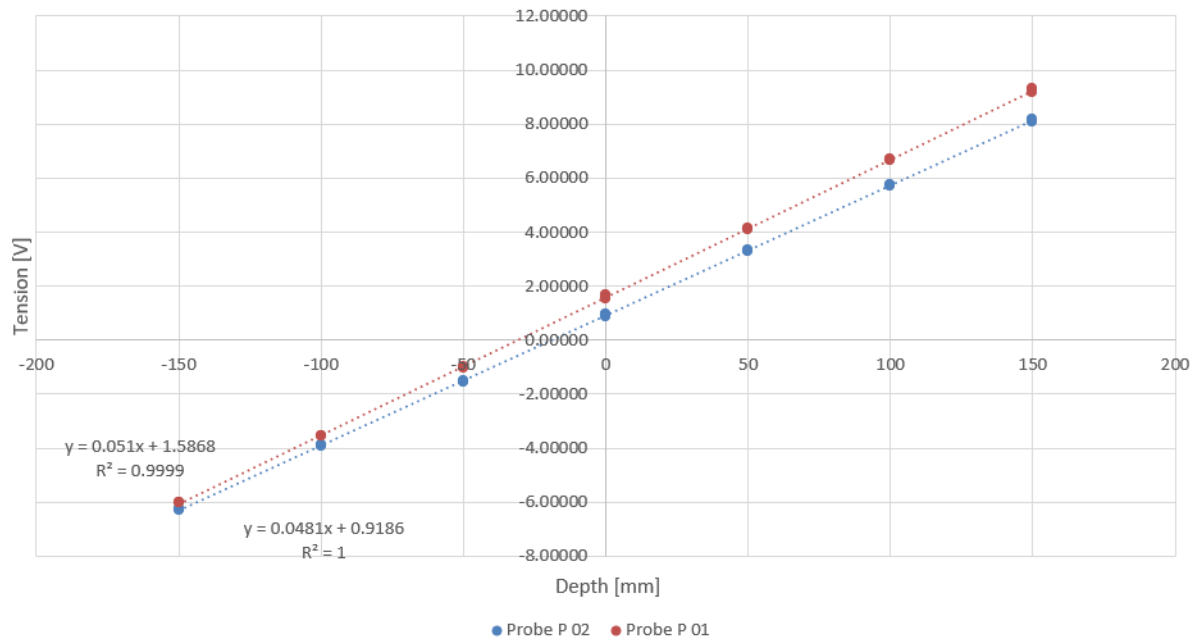


Figure 18: Wave probes calibration linear regression.

The results from the linear regression have then to be inputted in the acquisition program already installed in the carriage's computer.

4.2 Forces acquisition

In order to retrieve the data of the forces exerted on the mooring lines by the models, the mooring lines went through a hinged pulley and connected with a spring, itself connected on the other end to a load cell. Figure 19 shows the standard setup. In this chapter, the choice of the sensors, the data acquisition system (DAQ) to which it was connected, and the link between the sensor and the model will be reviewed.

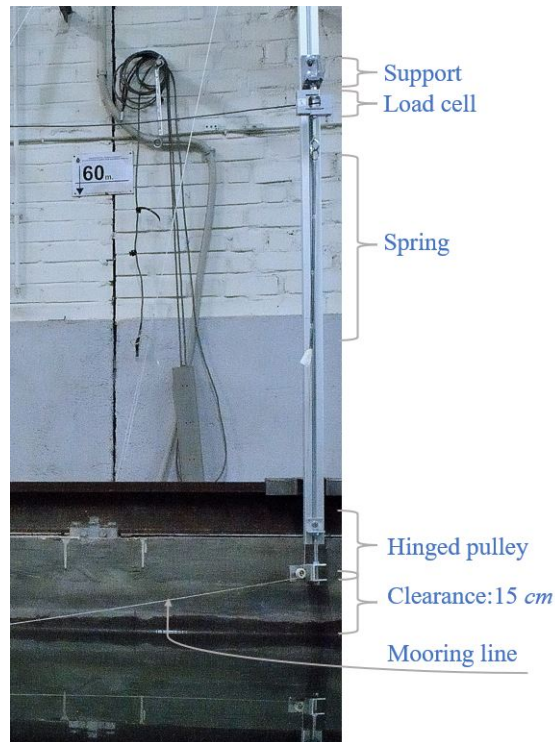


Figure 19: Load cells setup

4.2.1 Load cells

In the previous experiments performed on similar models, the recording of the forces encountered relevant difficulties. In fact, for the model that formed a 2-by-3 array, on a 1:60 scale, the resolution was too gross to record any useful data.

In that case, HBM U9C, load cells were used, coupled to a Spyder 8-30 acquisition system. They have the following characteristics:

- Spyder's ADC resolution: 16 bits
- Spyder's input range: $\pm 10V$
- U9C's force range: $\pm 200N$
- U9C's output signal: 0 to 10 V

We can then calculate the resolution of the system as follows:

$$Resolution = \frac{20000[mV]}{2^{16}[bits]} * \frac{\frac{400/1000[mN]}{9.81[m/s^2]}}{10[V]} = 1.24[g] \quad (3)$$

In order to tackle this problem, both the load cells and the acquisition systems were replaced for this campaign.

For the load cells, it was deemed prudent, since time was tight, to choose from the catalog of HBM, as their technology was well known in the towing tank laboratory in general.

First, it was decided to choose a cell load from the S2M series. Compared to the U9C series, they are much bulkier, and while their protection class is the same (IP67), they are susceptible to rust, which the U9C series are not. Since space in the assembly was clearly not a limitation, and the protection class was more than enough for this application, there were no practical downsides.

On the other hand, the S2M series were considerably cheaper, and are known to output less noisy data. Finally, it was observed that since the last campaign had readings close to the resolution of the acquisition system (depending on the wave, the data went from one to six steps), a load cell with a smaller range was chosen.

From HBM's catalog, three options were considered, in terms of the range of the load cell:

- $\pm 10 N$
- $\pm 50 N$
- $\pm 100 N$

In order to decide, the following simple reasoning was employed: for waves of height close to ours, the maximum force recorded was in the order of 2 grams. Our models had 56 modules instead of 6, and the biggest was close to four times bigger, so the force was multiplied by the number of modules' ratio, then scaled following Froude similarity, i.e. the cube of the ratio between the scales, as stated in Table 1:

$$F_{max} = 2[g] * \frac{56}{6} * \left(\frac{60}{15.5}\right)^3 \approx 1083[gf] \approx 10.6[N] \quad (4)$$

While this formulation is purely indicative, it already suggested that the 10 N alternative would not have been a prudent choice. The 50 N one was chosen instead.

On top of this, the DAQ was also replaced with a benchtop measurement system from National Instruments. A *CompactDAQ chassis* NI-cDAQ 9185 paired with a NI-9237 module was chosen, which has much better ADC resolution. They are both shown in Figure 20



Figure 20: Data acquisition system.

Summarizing, the new setup's characteristics were as follows:

- DAQ's ADC resolution: 24 bits
- DAQ's input range: $\pm 10 V$
- S2M's force range: $\pm 50 N$
- S2M's output signal: 0 to 5 V

We can then calculate the resolution of the system as follows:

$$Resolution = \frac{10000[mV]}{2^{24}[bits]} * \frac{\frac{100/1000[mN]}{9.81[m/s^2]}}{5[V]} = 1.23 * 10^{-3}[g] \quad (5)$$

In conclusion, resolution would no longer be a problem, although it is left to be seen whether noise will.

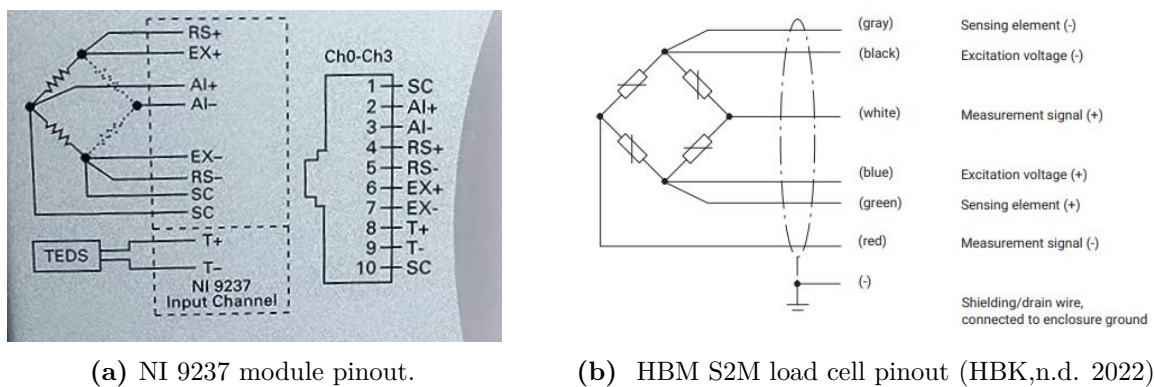
4.2.2 Connection of the DAQ

The new DAQ had to be connected on both ends. Downstream, towards the computer used, a simple Ethernet cable sufficed to make the link. To actually record the data, a LabVIEW program had to be used. It will be the theme of the next paragraph. Upstream, the choice of the NI 9237 module was also a good choice. As the load cells came with no connectors, they had to be installed by hand. As a first approach, a different module, that accepted RS 232 connectors was considered. As shown in Figure 21, the result was relatively not optimal, as the author's welding abilities are rather limited.



Figure 21: Welding of a load cell to a RS 232 connector.

The NI 9237 module, instead, accepts RJ50 connectors which are much simpler to install with the proper crimping tool. Figure 22 and Table 12 show the pin correlation that was followed for this.



(a) NI 9237 module pinout.

(b) HBM S2M load cell pinout (HBK,n.d. 2022).

Figure 22: Pin configuration of load cell and DAQ.

Table 12: RJ50 connection cables' color code.

Pin number	NI 9237 channel	Load cell color code	Load cell channel
1	SC	-	-
2	AI+	white	Measurement signal(+)
3	AI-	red	Measurement signal (-)
4	RS+	green	Sensing element (+)
5	RS-	gray	Sensing element (-)
6	EX+	blue	Excitation voltage (+)
7	EX-	black	Excitation voltage (-)
8	T+	-	-
9	T-	-	-
10	SC	-	-

Although much welding was avoided by the module choice, the cell load paced further from the bench required the extension of its connection cable, so some welding was unavoidable there.

4.2.3 *LabVIEW*

The data from the load cells was collected using NI's graphical programming environment, LabVIEW. The program's block view can be seen in Appendix A.

It must be mentioned that the program was not developed from scratch, but was largely based on an existing program created and kindly provided by Jon Martínez Carrascal, one of the Ph.D. students working in the CEHINAV laboratory. Through this program, all the reading parameters were set, like the acquisition time, the sampling frequency, and the relation between read voltage and corresponding force. On top of this, it was built so that the data not only would be saved into ASCII text files, but also displayed live in monitors in the front panel.

4.2.4 *Load cell calibration*

A program practically identical to the one presented in the previous paragraph was used. It was simplified for a single load cell.

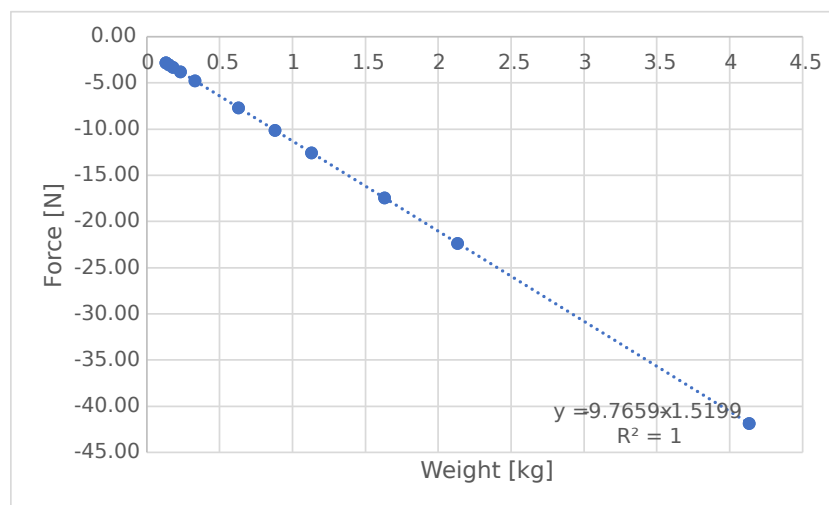
The procedure followed the same principle as that for the wave probes calibration. A series of eleven known weights would be hung from the fixed load cell twice. Knowing the forces applied, it was possible to make a linear correlation between the voltage read and the force applied to it.

With twenty-three measurements ranging from 1 to 40 newtons, the cell that showed the worst determination factor was of 99.9%. With this result, it was considered that the quality of the readings would be sufficiently warranted.

Table 13 and Figure 23, below, show the results for one of the load cells calibrated. Since the calibration was being performed, the results present a significant error. Nevertheless, the excellent linearity kept over the whole range of the sensor was an excellent result. The values of the trend line were the input for the program, in order to get a correct reading.

Table 13: Load cell S2M 832 calibration results.

Test number[-]	Weight [kg]	S2M 832 reading [N]
1	0.1312	-2.78
2	4.1312	-41.87
3	2.1312	-22.34
4	1.6312	-17.43
5	1.1312	-12.56
6	0.8812	-10.12
7	0.6312	-7.68
8	0.3312	-4.76
9	0.2312	-3.78
10	0.1812	-3.29
11	0.1512	-3.00
12	0.1312	-2.81
13	0.1512	-3.00
14	0.1812	-3.30
15	0.2312	-3.79
16	0.3312	-4.76
17	0.6312	-7.68
18	0.8812	-10.12
19	1.1312	-12.56
20	1.6312	-17.43
21	2.1312	-22.34
22	4.1312	-41.87
23	0.1312	-2.81

**Figure 23:** Load cell S2M 832 calibration linear regression.

4.3 Motion capture

A motion capture system (mocap), a technology used to digitally record the movement of objects, was used to collect data of the motions of the individual modules. In particular, the "OptiTrack" system was used.

The system included the following components:

- Small, reflective markers were attached in the middle of the panels. These markers reflect infrared light emitted by the cameras, allowing the system to determine their precise position in 3D space.
- 6 flex 13 optitrack high-speed cameras that can capture the motion of reflective markers placed on objects or individuals with great precision.
- Infrared Illumination: Infrared lights are used to illuminate the markers, making them highly visible to the cameras but not to the human eye. This minimizes interference and ensures accurate tracking. In our particular case, the infrared lighting was lodged in the cameras, around the lens.
- Capture Software: OptiTrack provides specialized software for setting up and calibrating the system, as well as for capturing and processing motion data.

In our configuration, each recorded module only carried one marker, in its center. Therefore, only translation degrees of freedom could be studied. The markers were positioned on top of 2 *cm* high columns made of light-weight polyurethane so that in the case water came on top of the module, the marker would not be obscured.

Not all the modules in the array were followed. Out of the seven-by-eight array, only the central five-by-six were studied. Figure 24 shows one of the models with the small columns for the marker placement.



Figure 24: Model c with markers.

5 MOORING LINES FORCE ANALYSES

This chapter will focus solely on the findings regarding the forces on the mooring lines of each model, for each test. In fact, from here on after, this report focuses on the work carried out after the tests were performed.

The campaign counted four waves per model. Each was run once (except for particular problem situations, in which the readings were discarded, and the waves re-ran), except the steepest wave of each scale, which was run 5 times, to check for repeatability.

The Matlab program found in Appendix C2 was used to process the data collected with the LabVIEW program in Appendix A. This program accesses the directory where the text files with the raw data are stored, and crosses it with a matrix that contains, for each of them, the boundaries of a specific interval. This interval was defined by a visual assessment of the time series, and to have a proper number of wave encounters (over 10). The whole signal passes through a low-pass filter, before having the peaks and troughs in the specific interval retrieved. The limit of the bandpass depends on the wave frequency of that specific test.

The filter is imperative. In fact, although the resolution of the forces acquisition system is very fine, as was shown in Chapter 4.2.1, the data presented significant noise levels. Figures 25 and 26 show the cleaned data superposed to the raw lecture from the load cell, for waves a1 and d1.

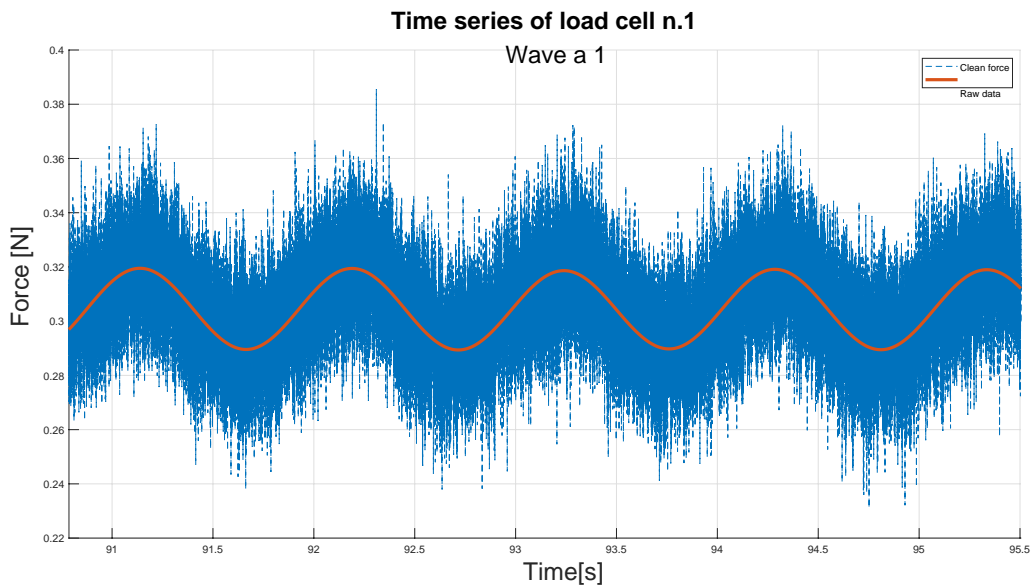


Figure 25: Raw versus clean data for line 1, test 1 a.

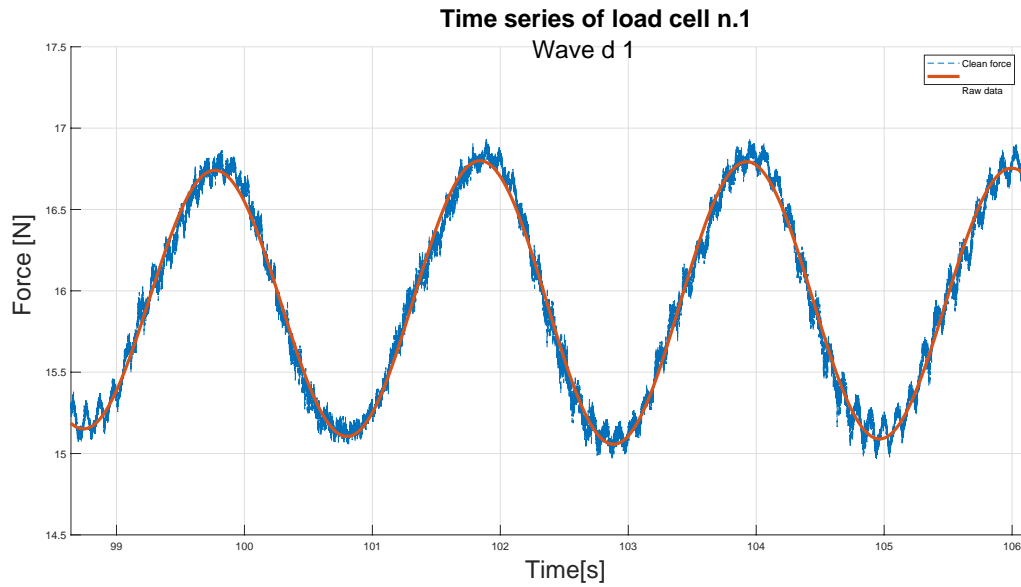


Figure 26: Raw versus clean data for line 1, test 1 d.

As can be seen, the low pass filter is such that it heavily impacts the time series. Nevertheless, the trend and amplitudes are clearly followed.

Figure 27 shows the filtered time series for each line for test 1 d.

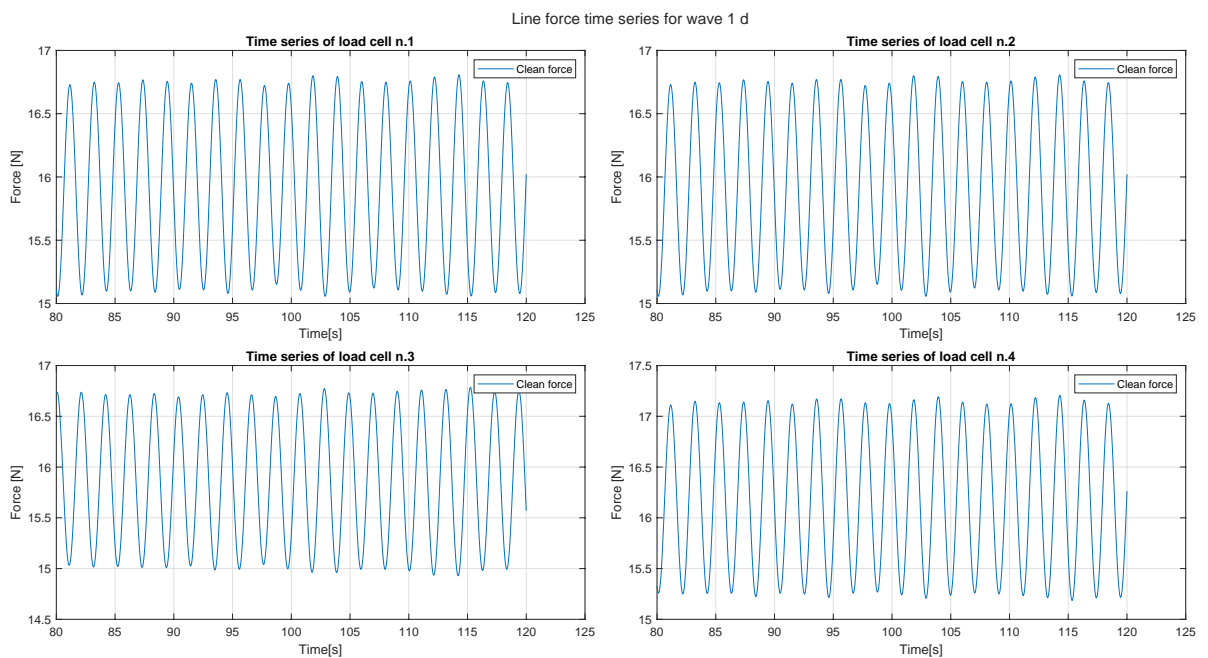


Figure 27: Clean time series of line forces for test 1 d

Finally, Table 14 lists the results for each wave. Only one value of force amplitude is shown for each wave. This is the average of that of each line. In the case of the steepest wave for each model, the value corresponds to the average of the five times that that same wave was run, and is accompanied by the standard deviation between the five tests.

Table 14: Summary of results from line force readings.

Wave	Scale	\widetilde{F}_M	\widetilde{F}_F	Standard deviation
[-]	[-]	[N]	[N]	[N]
d 1	1:15.5	1.86	6909	
d 2	1:15.5	1.68	6267	
d 3	1:15.5	1.52	5650	
d 4	1:15.5	1.37	5094	9.16
c 1	1:23.5	0.55	7075	
c 2	1:23.5	0.51	6604	
c 3	1:23.5	0.46	6024	
c 4	1:23.5	0.40	5241	25.76
b 1	1:43.8	0.077	6460	
b 2	1:43.8	0.074	6240	
b 3	1:43.8	0.066	5577	
b 4	1:43.8	0.059	4926	54.6
a 1	1:60	0.026	5694	
a 2	1:60	0.023	4882	
a 3	1:60	0.017	3713	
a 4	1:60	0.013	2773	72.45

Quite a few conclusions can be drawn from this data. First of all, it jumps to the eye that the less steep the wave is, the bigger the forces are. This suggests that we could be approaching a harmonic of the natural frequency of the system. In fact, looking back to Table 6, the less steep wave is rather close to the first subharmonic, according to our simple harmonic oscillator hypothesis.

Also, it can be seen that the smaller the model, the worse the repeatability is. This is not surprising, since all construction and mounting errors become more significant with smaller sizes. However, it is worth noting that even for the smallest model, the standard deviation suggests good repeatability.

Finally, the most important observation is that, for the three bigger models, there is no clear tendency that would suggest scale effects. Although the variations between those three models are significant, the results remain within a certain range, too. Opposed to this is the situation for the smallest model. In fact, this was expected: it was observed during the tests that a few factors seemed to have relevance for this model, but not for the others. First, the lines were clearly parabolic and often remained submerged after a wave was run. This can be seen in Figure 28 and suggests that the weight of the wet rope was not negligible for this model. Also, as will be shown in the analyses of its motions, this model was the only one to show relevant drift, indicating that the pretension was

insufficient to surpass the friction of the mounting.



Figure 28: Parabolic shape of mooring line in 1:60 scale model.

At last, the difference between the tension in the front and rear lines is compared in Table 15, as it will come in handy later.

Table 15: Front vs rear lines difference in tension amplitude.

wave	Front [N]	Back [N]	Difference [-]
d1	7153.580467	6663.734057	6.85
d2	6633.789731	5899.255538	11.07
d3	6142.475729	5157.223628	16.04
d4	5672.06828	4494.216241	20.77
c1	7468.118887	6702.825788	10.25
c2	7128.964094	6079.340475	14.72
c3	6673.890804	5373.588452	19.48
c4	5936.51149	4515.825355	23.93
b1	6422.16609	6497.172308	-1.17
b2	6367.923948	6112.167557	4.02
b3	5737.281106	5416.876065	5.58
b4	5206.743783	4721.638661	9.32
a1	6206.685573	5181.263446	16.52
a2	5446.380331	4317.991406	20.72
a3	4385.175719	3041.471449	30.64
a4	3550.130754	2113.427877	40.47

6 MOTIONS ANALYSES

In this chapter will be discussed the analyses of the different data obtained from the Optitrack. The first two sections will focus on the results from two series of decay tests. The later two sections tackle the analysis of the data recovered from the wave tests: Section 6.3 goes through different observations decanting from this data, while Section 6.4 deals with the amplitudes of the results.

6.1 Single panel decay tests

The first experiments performed were not carried out on the arrays, but rather on individual panels of the different scales. Each of them was equipped with four markers, one on each corner, which positions were recorded by the Optitrack, therefore allowing the total spatial identification of the panel. Of course, since there was no mooring system attached to it, only heave, roll and pitch could be studied.

As for other such models tested in the towing tank, the modules were taken out of their equilibrium position by hand. Nevertheless, due to the geometry of the modules, this did not offer good repeatability, as can be seen in Figure 29. For this reason five or six tests were performed for each scale and degree of freedom, for a total of seventy-six tests.



Figure 29: Execution of a decay test on a single panel.

The time series were inspected individually, resulting in the discard of twenty-one of them. From the remaining tests, the peaks and periods were extracted, and their average was calculated, after being extrapolated to full scale. Figure 30 shows the angle of the plane formed by the markers with respect to the vertical. Figures 31 through 33 show the results found. In particular, they show for each scale and degree of freedom the average period and amplitude of the oscillations.

The precise calculations can be seen in Appendix C3, where the whole code for the analysis of the data recovered from these tests is displayed.

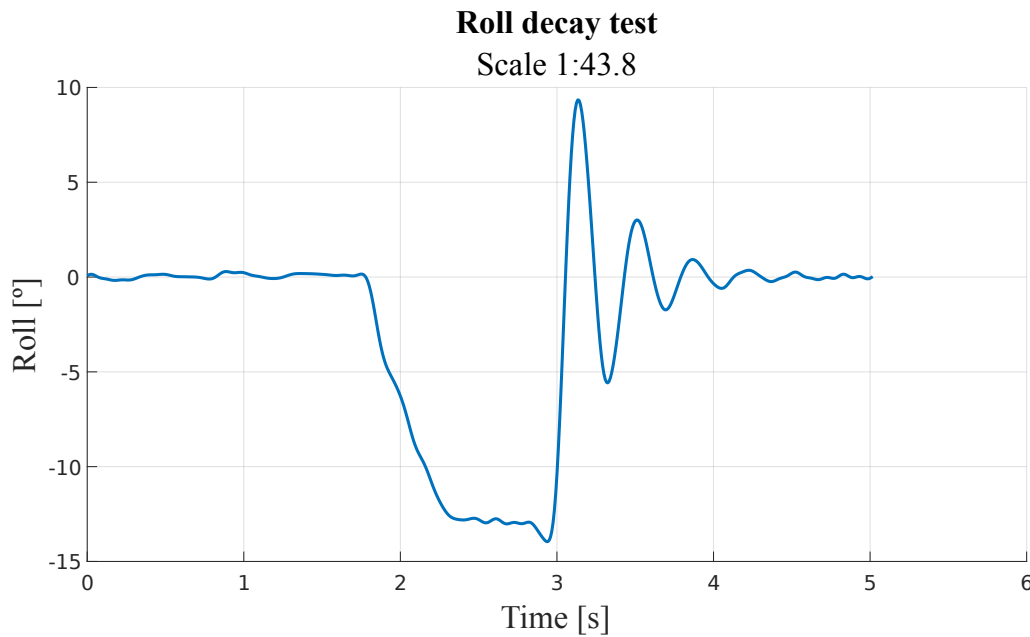


Figure 30: Time series of roll decay test.

Before drawing any conclusions, though, as the previous results were fairly scattered, interest was taken into checking the distribution of every single considered oscillation. The results are also reported in the abovementioned Figures.

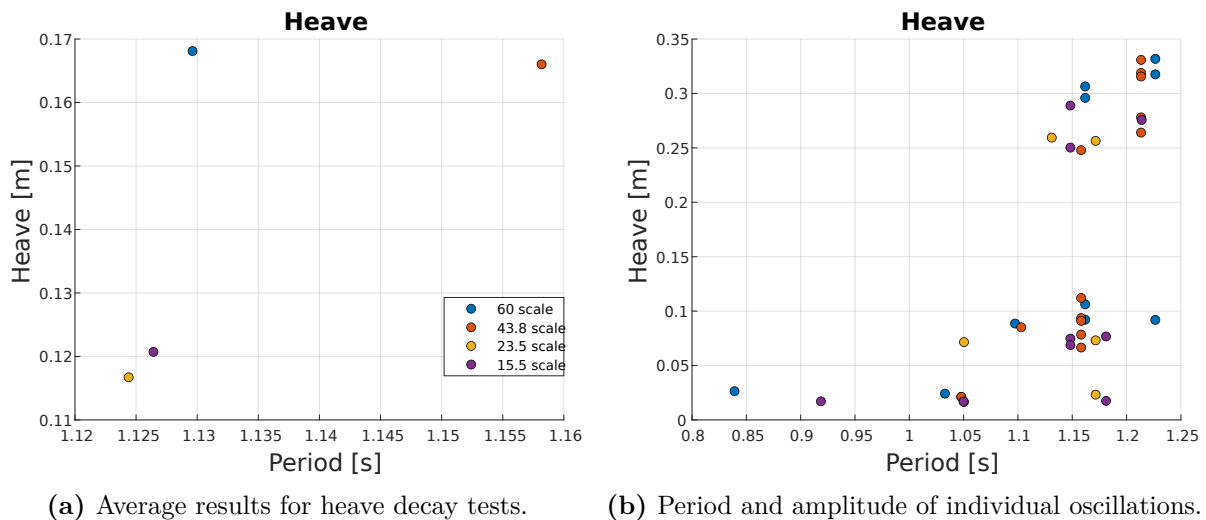


Figure 31: Decay tests in heave overview.

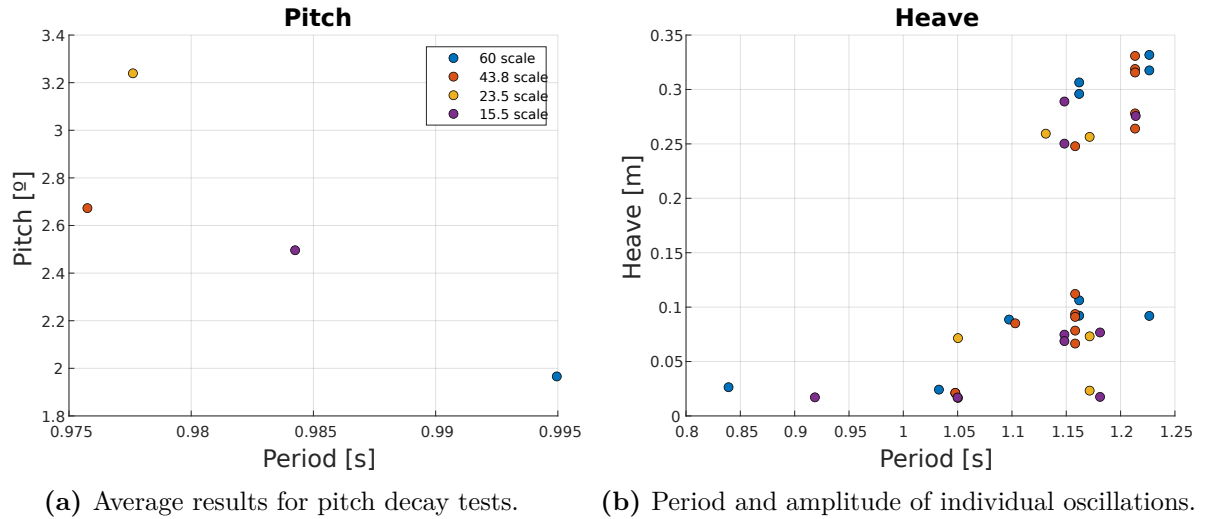


Figure 32: Decay tests in pitch overview.

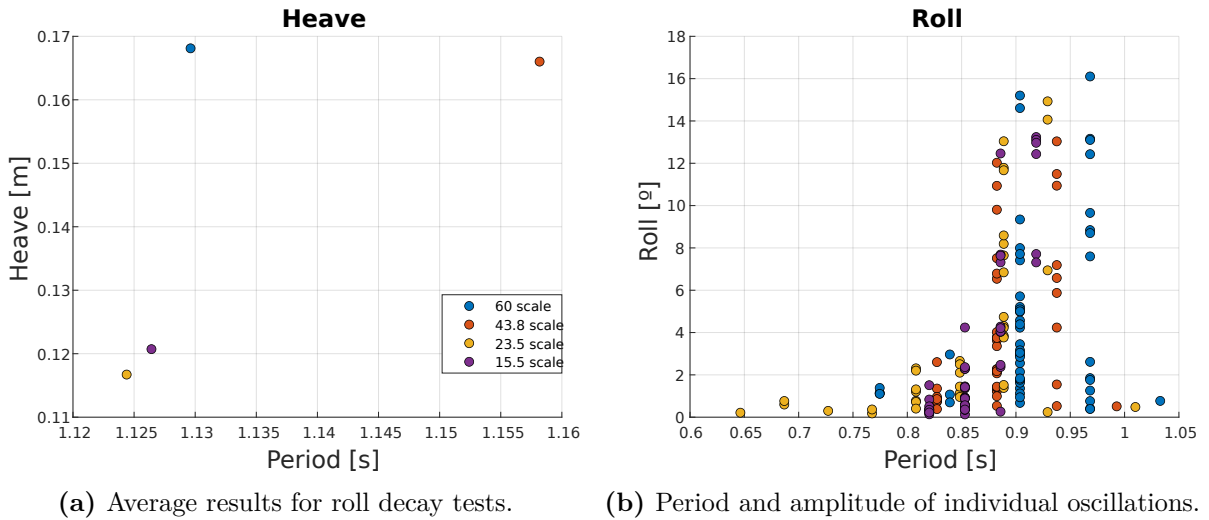


Figure 33: Decay tests in roll overview.

Since the results are heavily scattered, a different alternative for their analysis was chosen: the damping ratio between the two first peaks of each valid test was calculated through the logarithmic decrement method.

The damping ratio, with this method, is calculated as follows:

$$\delta = \frac{1}{n} \ln \frac{x(t)}{x(t+nT)} \quad (6)$$

$$\zeta = \frac{\delta}{\sqrt{4\pi^2 + \delta^2}} \quad (7)$$

With:

- $x(t)$: the amplitude
- n : the number of periods between peaks

- T : the period of the oscillation

Table 16, below, shows the results found from this approach.

Table 16: Damping ratios by scale and degree of freedom.

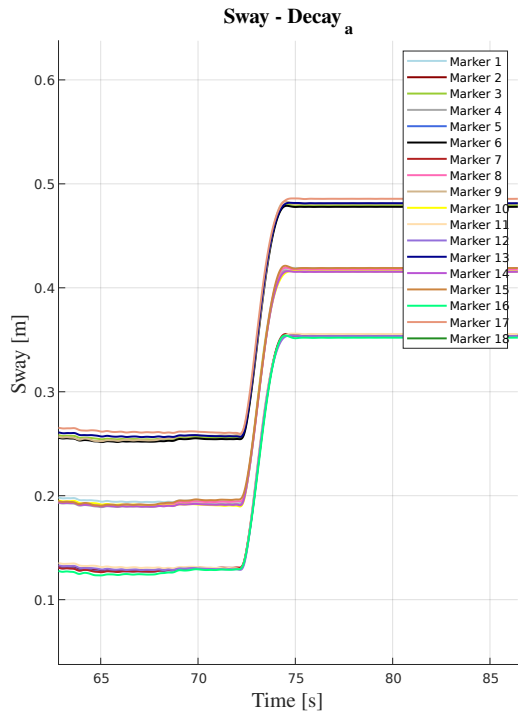
Scale	Heave [-]	Pitch [-]	Roll [-]
60	0.187	0.088	0.081
43.8	0.189	0.097	0.083
23.5	0.198	0.098	0.085
15.5	0.204	0.095	0.085
Standard deviation	0.0078	0.0043	0.0020

Two contrasting observations can be made from these results. On one hand, the damping ratio seems to grow consistently with the scales for all three degrees of freedom. On the other hand, the results are quite close together, as show the standard deviation for each DOF.

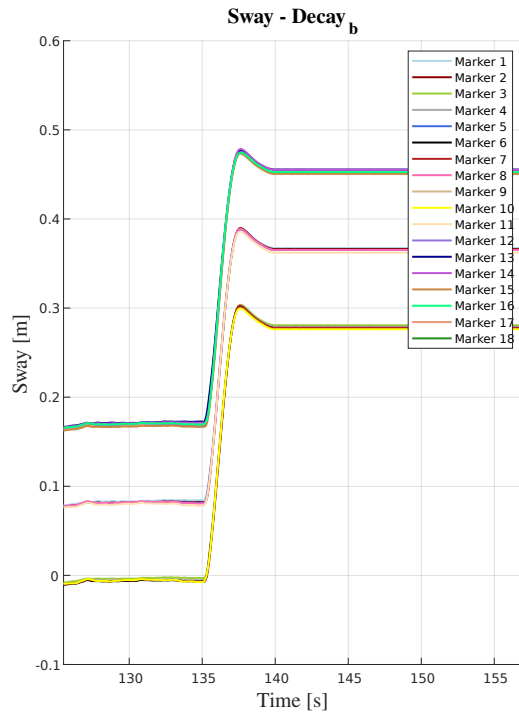
6.2 Array decay tests

Before each set of tests, with the model setup for as shown in Figure 24, decay tests were performed on the array models. Due to their multi-body nature, roll, pitch, yaw and heave were impossible to study. Therefore, only surge and sway decay tests were performed. For each of them, three repetitions were carried out.

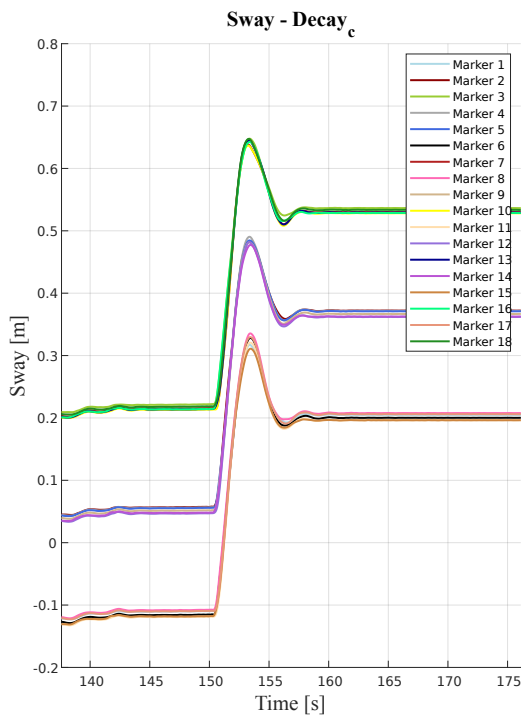
In this case, since the results were quite difficult to treat, but relatively easy to spot, it was preferred to conduct a qualitative analysis. For each test, the time series were filtered, then the cleanest repetition was chosen and reported on Figures 34 and 35. It is worth noting that while the readings in sway for the biggest array are not great, they allow a simple characterization of the response as on that presents a few oscillation, which is enough for this analysis.



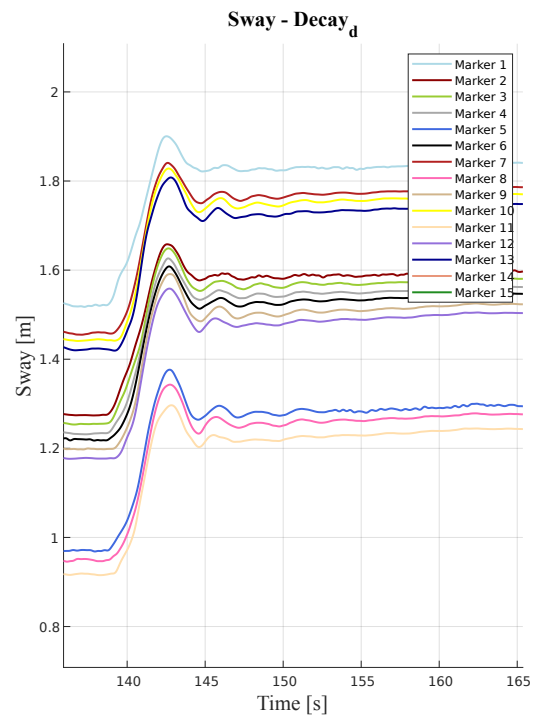
(a) 1:60 scale array decay test.



(b) 1:43.8 scale array decay test.

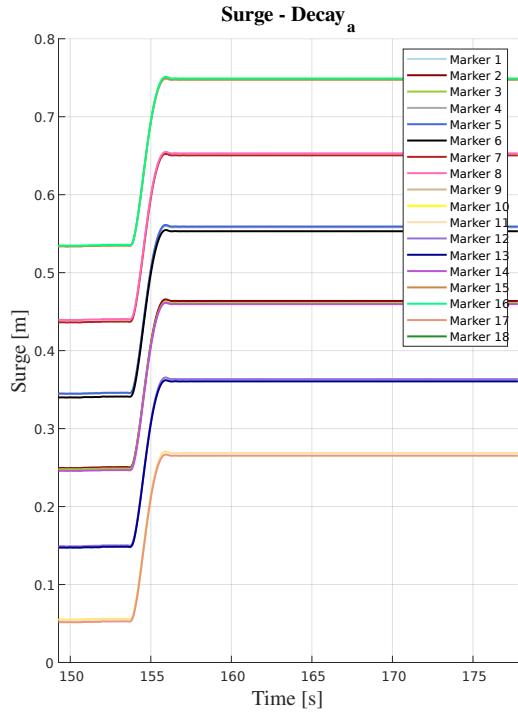


(c) 1:23.5 scale array decay test.

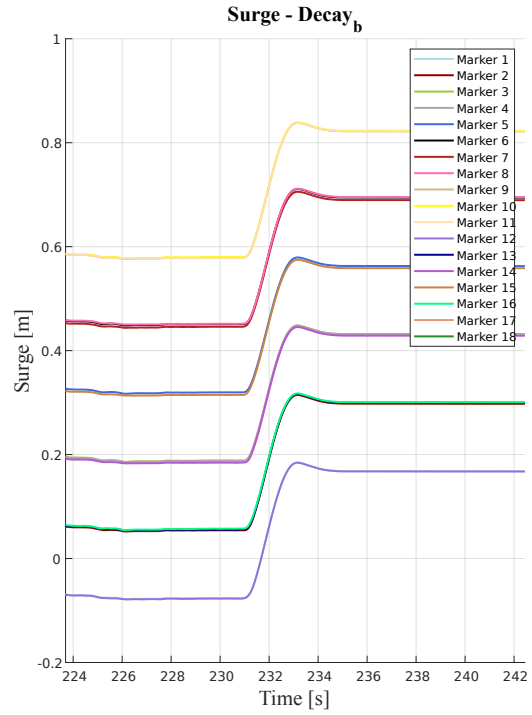


(d) 1:15.5 scale array decay test.

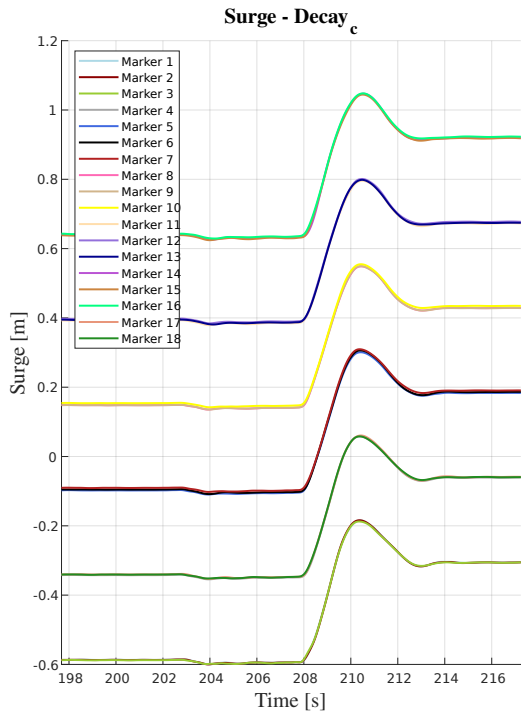
Figure 34: Sway decay tests on array models.



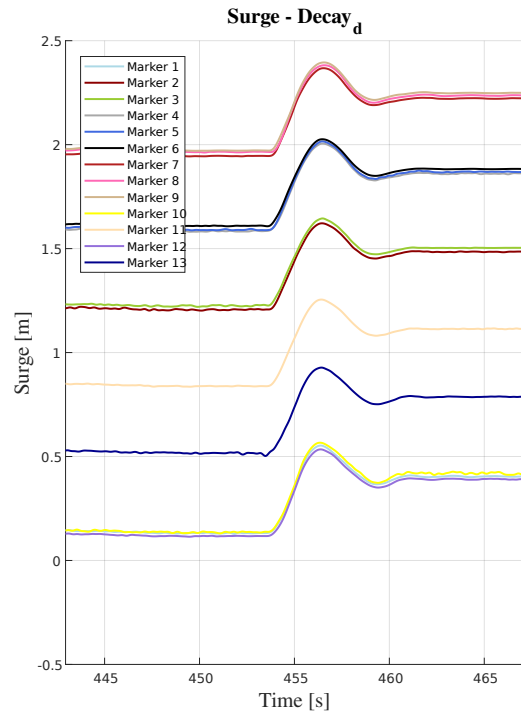
(a) 1:60 scale array decay test.



(b) 1:43.8 scale array decay test.



(c) 1:23.5 scale array decay test.



(d) 1:15.5 scale array decay test.

Figure 35: Surge decay tests on array models.

Table 17: Observations on array decay tests.

Scale	Sway	Surge
1:60	Close to critically damped	Close to critically damped
1:43.8	Slightly underdamped, shows only one peak	Slightly underdamped, shows only one peak
1:23.5	Shows up to three peaks	Shows a small second peak
1:15.5	Shows a few peaks	Shows up to a third peak, although quite small

Table 17, above, collects the observations for each test. Unlike in the precedent decay tests, performed on the single model, here, a trend in which the smaller the model the more damped it is is evident.

Let's take the example of the logarithmic decrement method of calculating the damping ratio: as shown in Equation 7, the damping ratio depends only on the logarithmic decrement, which itself depends only on the ration between the amplitudes of two consecutive peaks. The amplitudes, though, should scale linearly with Froude similarity. Therefore, these results indicate that this property is not found between these models.

Another observation to consider is that, as explained in the previous Chapter 5, the smaller model seems not to be taut enough to overcome the internal friction of the system. This aspect will be commented further.

6.3 Wave tests observations

From here on after, the time series obtained from the wave tests are treated.

The first detail that had to be tackled when confronting the wave tests data was that the optitrack occasionally lost track of one or more markers, resulting in a mix of the signals. It was then necessary to sort them out individually, in order to get the proper time series for each marker. This was extremely time-consuming. Figure 36 shows an example of this phenomenon.

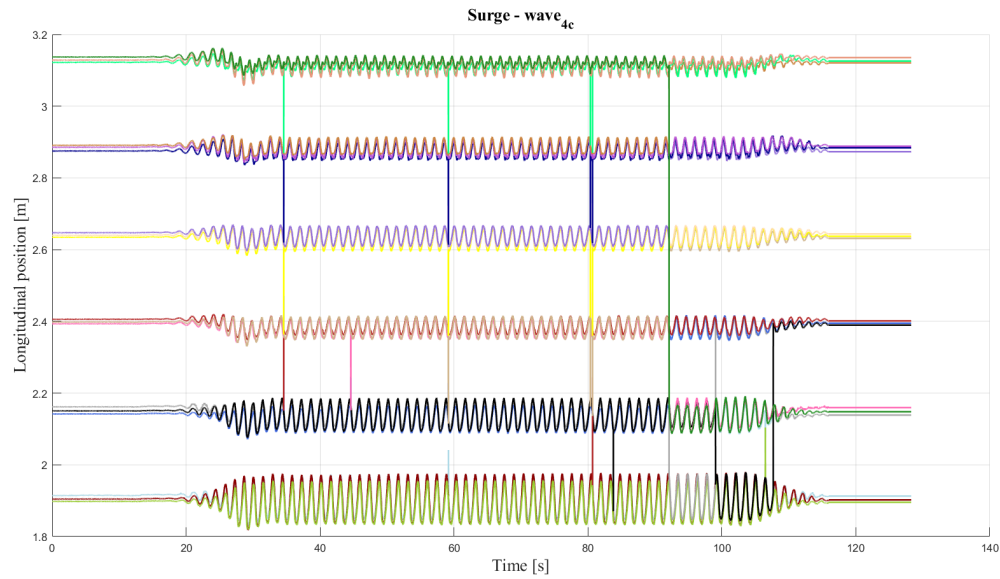


Figure 36: Raw time series from wave 4 c.

This example was fixed. Unfortunately, some files were much more damaged. For this reason, for tests 4 c and 4 d, only one of the repetitions was kept. The smaller models, instead, only rarely presented this problem, so the repetitions were kept without difficulties. Consequently, the check the repeatability of the tests had to be abandoned on the motions. Nevertheless, the excellent repeatability shown by the analysis of the forces should suffice. Once the time series were corrected, they underwent a bandpass filter, which window was centered in the frequency of the wave tested. Figure 37 shows, as an example, the effect of such filtering in the surge time series of on of the markers, during test 1 c.

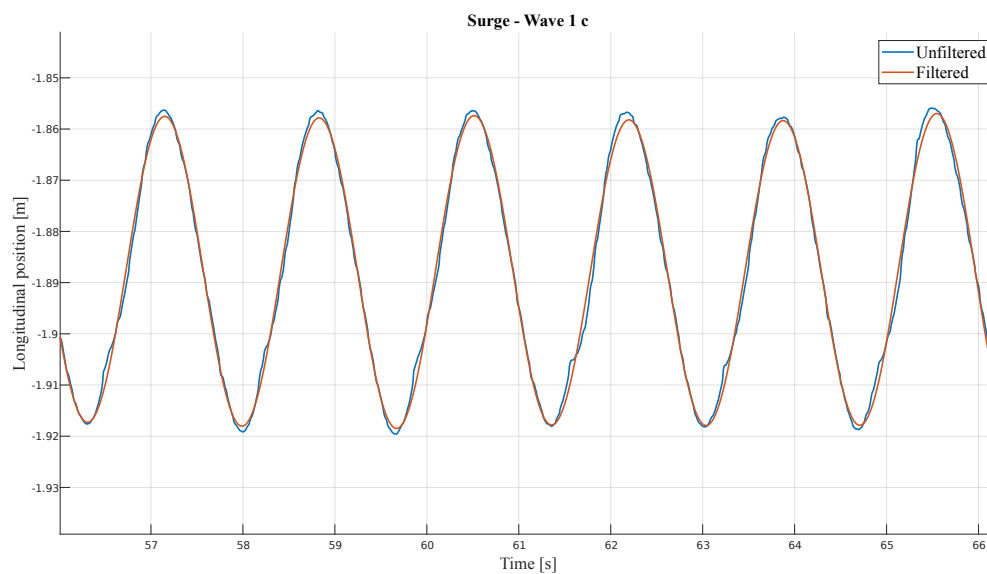


Figure 37: Raw vs. filtered time series in surge for test 1c.

The filter was kindly extended by professor Saettone, and can be seen in Appendix C4. It works by implementing a Gaussian window in the frequency domain.

At this point, in order to determine the amplitude of the motions, two more small considerations had to be made:

First, the numbering of the markers was relatively random, as can be seen in Figure 38. This was not a problem for computing the motions in heave, for which all the markers are evaluated together, but becomes one for the other two degrees of freedom, as there was an interest in studying subsets of the markers. To tackle this, the initial position of each of the recordings was manually registered.

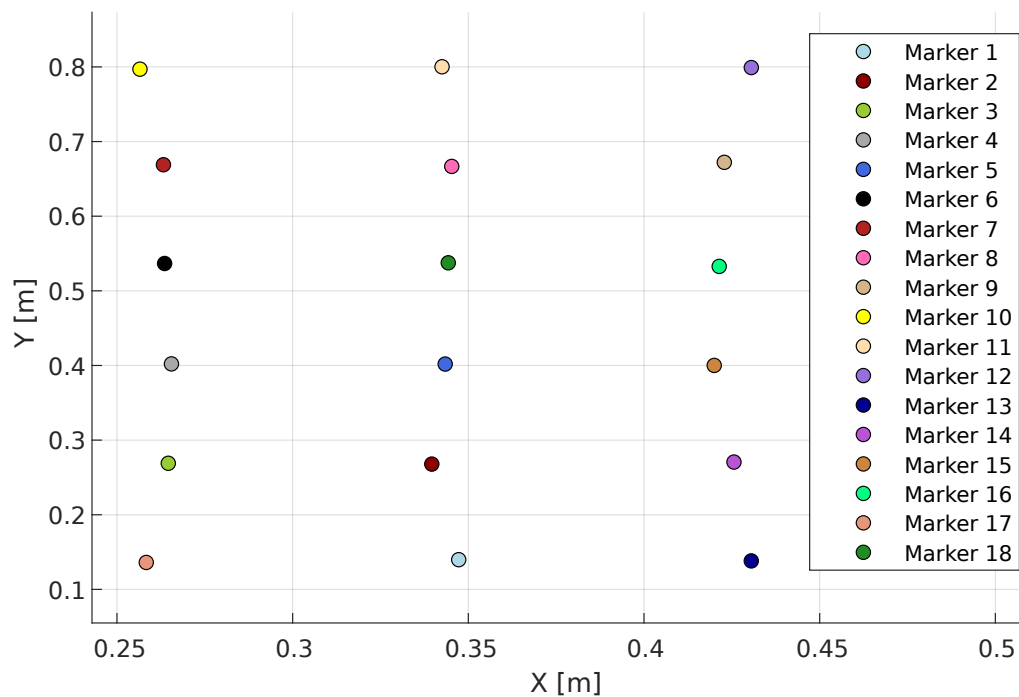


Figure 38: Initial position of markers for wave 2b.

Secondly, when changing the setup between the two models, the Optitrack cameras had to be re-positioned to better aim towards the markers. This operation required to redo also the calibration of the system. For this procedure, a tool with three markers served to define the coordinate system. Unfortunately, it got rotated of 90° between the first and second series of tests, which meant that particular attention had to be given to which degree of freedom one was working with.

Looking back to Figure 36, it can be seen that the later a row of modules encountered the wavefront, the smaller the response was. This can be related to the results shown in Table 15, where it can be seen that the tension on the front mooring lines is not only higher, but also presents higher variations than those on the rear of the model. Similarly, for the motions in sway, out of the three columns of modules with markers, the two side

ones were symmetrical, and oscillated with the same frequency as the waves tested. The central column, instead, did not show relevant data, as shows Figure 39.

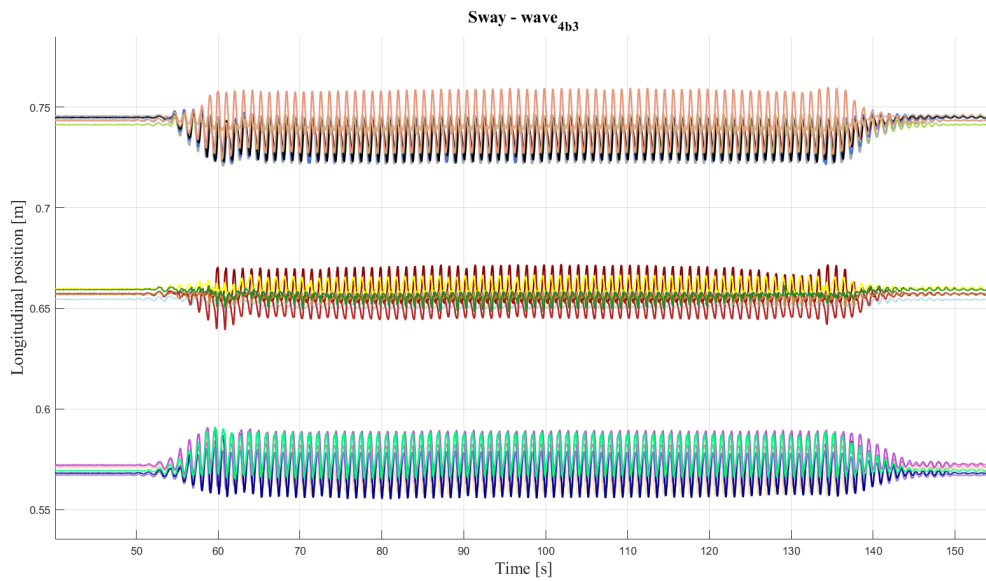


Figure 39: Sway time series from test b 4 (third repetition).

Another phenomenon observed was that displayed in Figure 40.

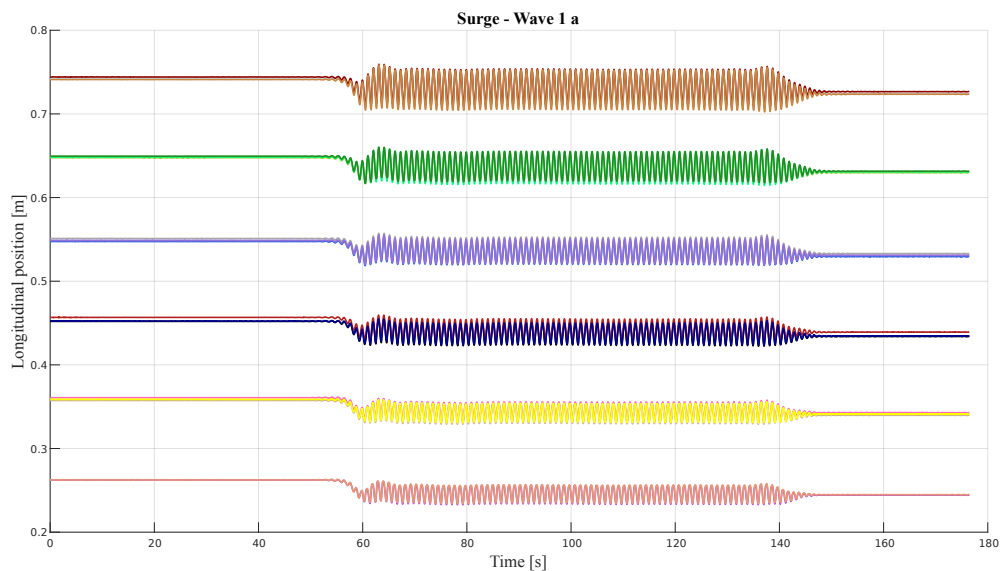


Figure 40: Surge time series from test a 1.

As anticipated in the previous chapter, for the smallest model, the pretension was set too low to overcome the mechanical friction of the mounting system. It can be seen in Figure 40 that all markers first experience a particular transient. Furthermore, the resting positions before and after the test had changed.

6.4 Motions analyses results

Once the data was fixed, sorted and filtered, the core of the analysis was tackled. For this purpose, a window of time was defined for each test, such that it contained at least ten wave encounters, as per ITTC recommendations, and that the peaks did not show any abnormalities. From these intervals, the peaks were extracted, and the amplitudes computed in the different degrees of freedom studied. The results were then extrapolated to full scale. Seeking to avoid overloading the annex, this program has not been attached, since it re-utilized the different techniques already employed in the other programs reported.

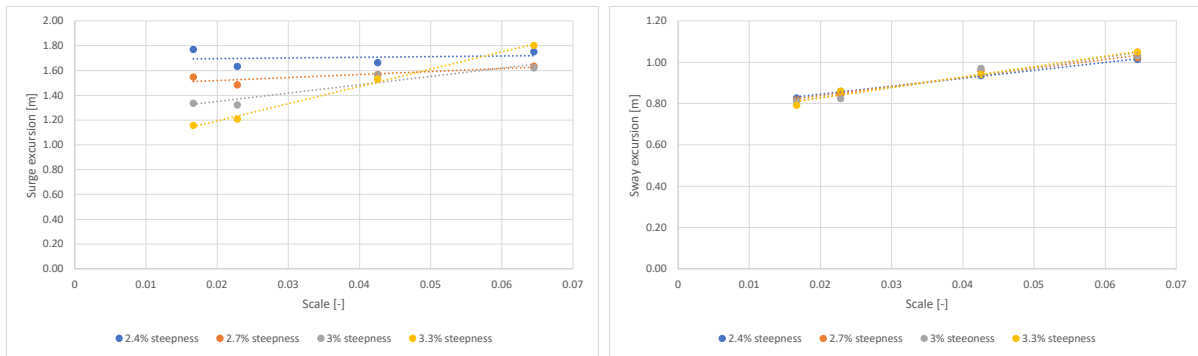
6.4.1 General approach

As a first approach, the full scale results were averaged into a single value per degree of freedom per test. Table 18 shows a summary of the results found for each test.

Table 18: Summary of main results.

Test	Scale	Sway	Surge	Heave
[-]	[-]	[m]	[m]	[m]
1 a	1:60	0.83	1.77	2.63
2 a	1:60	0.82	1.55	2.50
3 a	1:60	0.81	1.34	2.46
4 a	1:60	0.79	1.16	2.42
1 b	1:43.8	0.86	1.63	2.41
2 b	1:43.8	0.85	1.49	2.46
3 b	1:43.8	0.82	1.32	2.50
4 b	1:43.8	0.86	1.21	2.47
1 c	1:23.5	0.94	1.66	2.49
2 c	1:23.5	0.96	1.57	2.57
3 c	1:23.5	0.97	1.57	2.59
4 c	1:23.5	0.94	1.53	2.39
1 d	1:15.5	1.01	1.75	2.49
2 d	1:15.5	1.02	1.64	2.49
3 d	1:15.5	1.03	1.62	2.48
4 d	1:15.5	1.05	1.80	2.50

Figure 41 shows the results in function of the scale, for each different wave steepness tested.



(a) Surge excursion depending on model scale and (b) Sway excursion depending on model scale and wave steepness.

Figure 41: Excursions in surge and sway as a function of the scale, for different wave steepness values.

From these results, the observations that can be made for each degree of freedom are fairly different. In heave, it would seem as if no scale effects were present. This is true, but also banal: since the wavelength of the waves run was always much longer than the individual modules, they followed the wave elevation tightly. Nevertheless, this does not make the evaluation of the heave useless, as it is an indicator of the quality of the tests.

In surge, the results are considerably scattered. This is probably due to the uncertainties related to the model. However, excepted the less steep wave, there is a tendency for which the bigger the model is, the greater the response. And the steeper the wave, the more this is exacerbated.

In sway, the same tendency is not only present, but much clearer. This is an apparent evidence of the presence of scale effects.

6.4.2 Detailed approach

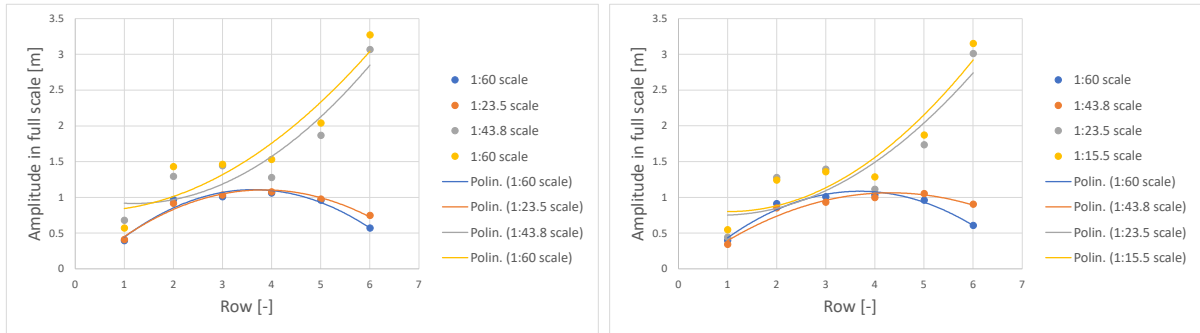
After this general approach, couple more analysis were carried out in order to provide further observations.

As mentioned at the beginning of this Chapter, the surge excursion decreases with every row, the further they are from the wave generator. In sway, though, this observation was less obvious. It was therefore considered interesting to check whether this was also the case in sway, and whether the trends found earlier when averaging all the markers were maintained when comparing row-by-row.

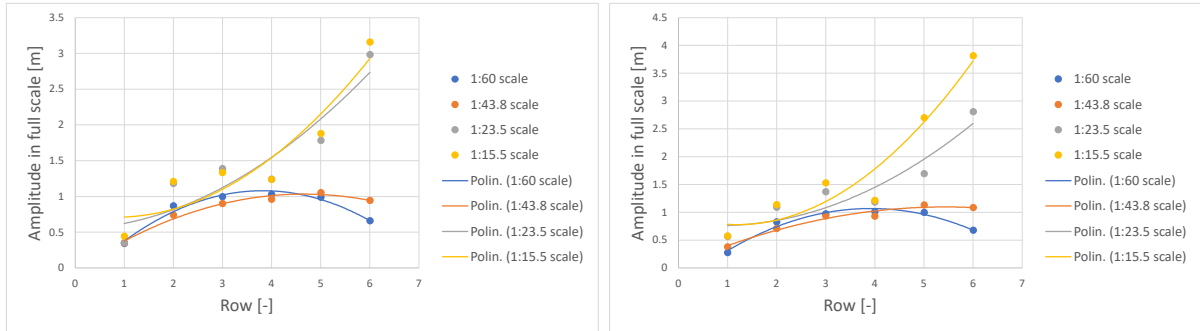
For this analysis, the average amplitude of the response in surge of the three markers of each row was considered in full scale. In sway, the same procedure was followed, omitting the central markers, for the same reason as before.

The results are reported in sway and surge are reported in Figures 42 and 43, respectively. For the sake of clarity, the results are displayed in the same graphs only for results corresponding to similar waves. The Figures show the the average amplitude for each row and for each

scale. It was chosen to accompany the results with second degree polynomial trendlines, as they adapt better to the trends represented.

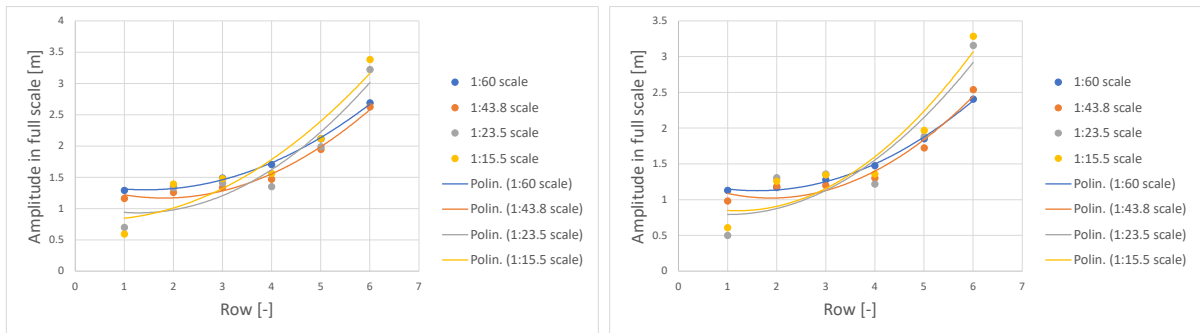


(a) Sway, row-by row, for Wave 1 (2.4% steepness) (b) Sway, row-by row, for Wave 2 (2.7% steepness)

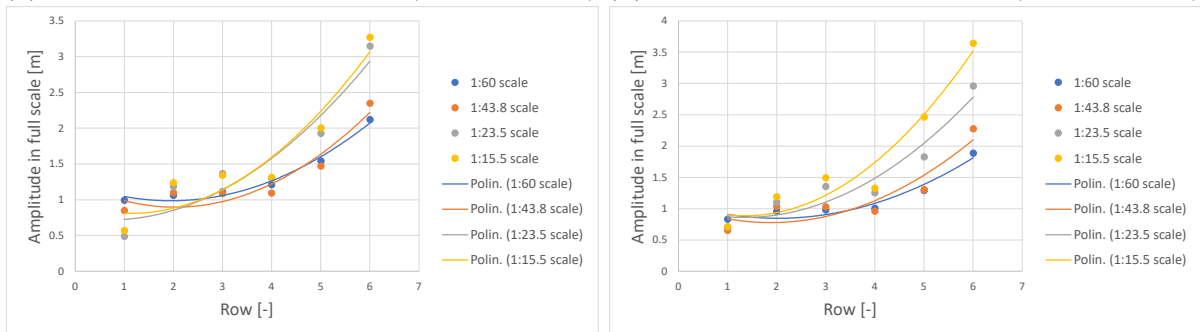


(c) Sway, row-by row, for Wave 3 (3.0% steepness) (d) Sway, row-by row, for Wave 4 (3.3% steepness)

Figure 42: Sway average amplitude by row.



(a) Surge, row-by row, for Wave 1 (2.4% steepness) (b) Surge, row-by row, for Wave 2 (2.7% steepness)



(c) Surge, row-by row, for Wave 3 (3.0% steepness) (d) Surge, row-by row, for Wave 4 (3.3% steepness)

Figure 43: Surge average amplitude by row.

As can be seen, while in surge there is a certain consistency, the tendencies in sway heavily differ between the two smaller and the two bigger models. Such differences in behavior help confirm the presence of scale effects. between these scales.

Finally, it was also deemed interesting comparing the results in surge between the central column and the laterals, to get a grasp of the coupling effect between sway and surge in this experiment. Table 19 shows the comparison of these results.

Table 19: Central vs. lateral results in surge

Wave	Lateral [m]	Central [m]	Relative difference [-]
1 a	1.72	1.81	4.8
2 a	1.51	1.60	5.8
3 a	1.30	1.38	6.1
4 a	1.14	1.20	4.7
1 b	1.54	1.69	8.7
2 b	1.36	1.55	12.0
3 b	1.17	1.41	16.5
4 b	1.06	1.26	15.7
1 c	1.63	1.79	8.9
2 c	1.49	1.72	13.0
3 c	1.49	1.73	13.9
4 c	1.46	1.69	13.7
1 d	1.72	1.82	5.6
2 d	1.49	1.76	15.0
3 d	1.53	1.78	14.2
4 d	1.79	1.75	-2.0

As can be seen, surge tends to be significantly more important in the central column, as important sway seems to restrict this movement to some extent. It is also noticeable that with the exception of the smaller model, there seems to be a considerable consistency between the different scales, excepted test 4d, which is considered an outlier.

7 Conclusions

This document presents the study of scale effects in models of the concept design RecSolar, of a floating photovoltaic plant. For this scope, four models of different scales were built and tested for different waves in the towing tank of the CEHINAV, at the *Universidad Politécnica de Madrid*.

The different stages of the experiment are displayed, from the motivations behind the realization, to the design of the experiments and models, their construction, execution and finally, the analysis of the results.

Two different kinds of data were retrieved from the experiments: the tensions in the mooring lines and the motions of a significant part of the panels.

From these analyses, the following conclusions can be drawn:

- On top of hydrodynamic effects, mechanical friction was not negligible for the smaller model, which difficult the extrapolation of its results. This is reflected on the results from the forces on the different models, which would not suggest important scale effects otherwise.
- Decay tests performed on the single panels of the different scales already show signs of scale effects being present on the models.
- Decay tests on the arrays further confirm this, showing considerable differences in the damping ratios for the different scales.
- The analysis of the responses reveals that in sway, a certain tendency of the results to show greater excursions for the bigger models is remarked.
- This remark is confirmed by the analysis in surge, where this tendency is much clearer.
- Finally, a comparison of the results in sway and surge for the different rows and columns of modules show further examples of different behavior of the models.

Given the binary nature of the issue studied, a final binary conclusion is corresponding: The different tests and observations performed on the models show that both hydrodynamic and mechanical effects on the systems result in the presence of scale effects.

References

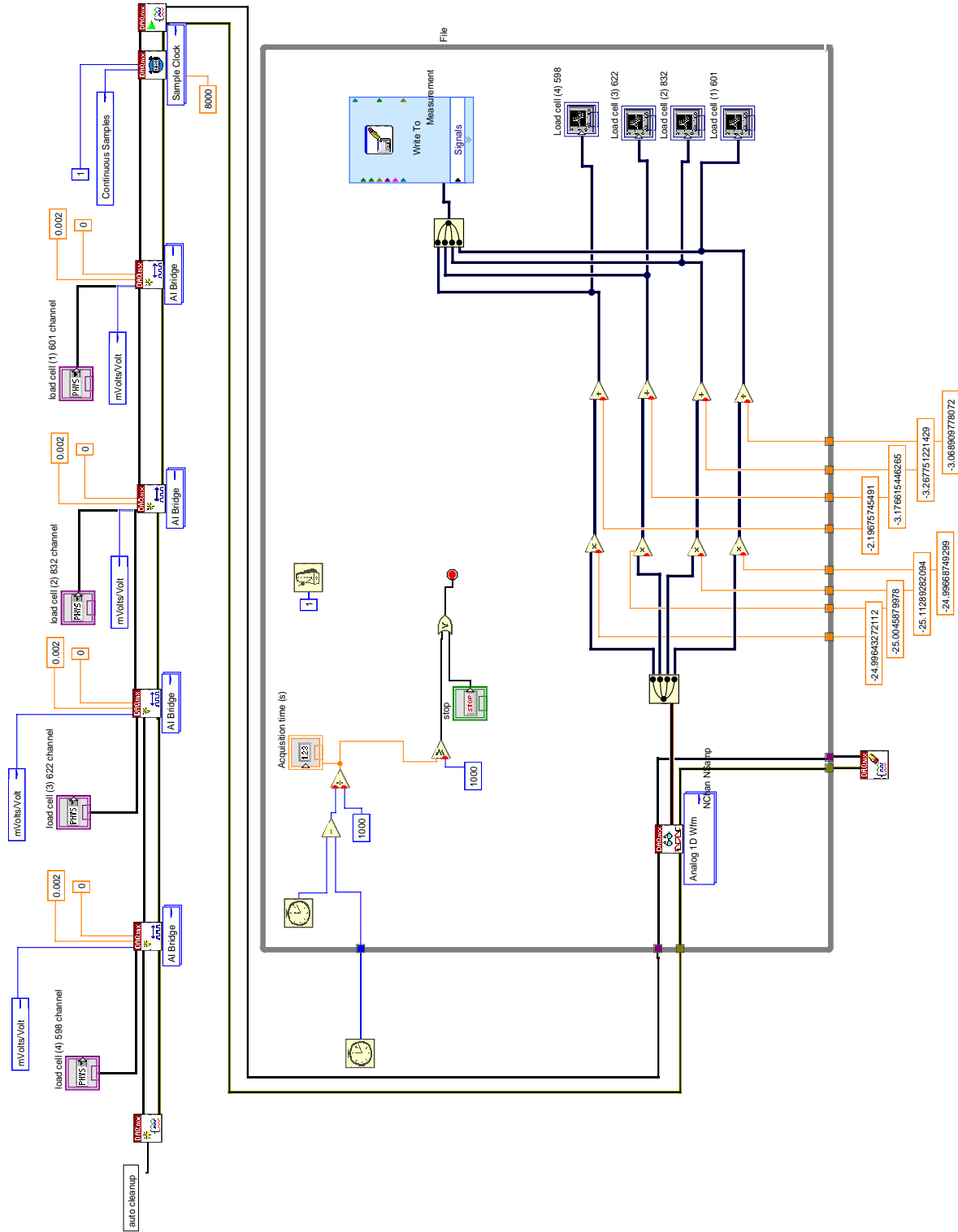
- [1] United Nations Framework Convention on Climate Change, UNFCCC, 2015, *PARIS AGREEMENT*, https://unfccc.int/sites/default/files/resource/parisagreement_publication.pdf
 - [2] IPCC. (2022). Global Warming of 1.5°C: IPCC Special Report on impacts of global warming of 1.5°C above pre-industrial levels in context of strengthening response to climate change, sustainable development, and efforts to eradicate poverty (1st ed.). Cambridge University Press. <https://doi.org/10.1017/9781009157940>
 - [3] UN, 2022, *The Sustainable Development Goals Report*, Department of Economic and Social Affairs Statistics. <https://unstats.un.org/sdgs/report/2022/The-Sustainable-Development-Goals-Report-2022.pdf>
 - [4] Conti, J., P. Holtberg, J. Diefenderfer, A. LaRose, J. T. Turnure and L. Westfall (2016). *International energy outlook 2016 with projections to 2040*, USDOE Energy Information Administration (EIA), Washington, DC, United States. Source: [https://www.eia.gov/outlooks/ieo/pdf/0484\(2016\).pdf](https://www.eia.gov/outlooks/ieo/pdf/0484(2016).pdf)
 - [5] Dorte Nørgaard Madsen, Jan Petter Hansen, Outlook of solar energy in Europe based on economic growth characteristics, *Renewable and Sustainable Energy Reviews*, Volume 114, 2019, 109306, ISSN 1364-0321, <https://doi.org/10.1016/j.rser.2019.109306>.
 - [6] World Bank Group, ESMAP and SERIS. 2019. Where Sun Meets Water: Floating Solar Market Report. Washington, DC: World Bank. Source: https://www.seris.nus.edu.sg/doc/publications/ESMAP_FloatingSolar_TEXT-A4-WEB.pdf
 - [7] Raniero Cazzaniga, Marco Rosa-Clot, The booming of floating PV, *Solar Energy*, Volume 219, 2021, Pages 3-10, ISSN 0038-092X, <https://doi.org/10.1016/j.solener.2020.09.057>.
 - [8] Zhiyu Jiang, Jian Dai, Simone Saettone, Glenn Tørå, Zhao He, Musa Bashir, Antonio Souto-Iglesias, Design and model test of a soft-connected lattice-structured floating solar photovoltaic concept for harsh offshore conditions, *Marine Structures*, Volume 90, 2023, 103426, ISSN 0951-8339, <https://doi.org/10.1016/j.marstruc.2023.103426>
 - [9] Méhauté, B.L., 1969. *An Introduction to Hydrodynamics and Water Waves* Pacific Oceanographic Laboratories. U.S. Department of Commerce, Environmental Science Services Administration <https://books.google.es/books?id=7Ir6rQEACAAJ>
 - [10] G. Bongiovanni, G. Roccati, 1994 *Le molle - tipi e criteri di calcolo*, Torino, Levrotto & Bella.
-

-
- [11] W. Froude, 1879, *The Laws of Fluid Resistance*, Science Lectures at South Kensington. Vol. II. London: Macmillan Company.
- [12] Pereya, B. T., Z. Jiang, Z. Gao, M. T. Anderson and H. Stiesdal (2018). Parametric Study of A Counter Weight Suspension System for the Tetraspar Floating Wind Turbine. Proceedings of the ASME 2018 International Offshore Wind Technical Conference, IOWTC 2018, San Francisco, USA.
- [13] DNVGL (2018). Standard DNVGL-ST-0119 Floating wind turbine structures.
- [14] ITTC, (2021a). Recommended Procedures and Guidelines: Floating Offshore Platform Experiments, International Towing Tank Conference, Vols. 7.5-0.2-07-03.1, 2021.
- [15] ITTC, (2021b). Recommended Procedures and Guidelines: Guideline for Model Tests of Stationary Multi-Bodies Operating in Close Proximity, International Towing Tank Conference, Vols. 7.5-02-07-03.1.
- [16] ITTC, (2002). Testing and Extrapolation Methods Loads and Responses, Ocean Engineering Analysis Procedure for Model Tests in Regular Waves, International Towing Tank Conference, Vols. 7.5-02-07-03.2
- [17] ITTC, (2017). Passive Hybrid Model Tests of Floating Offshore Structures with Mooring Lines, International Towing Tank Conference, Vols. 7.5-02-07-03.5
-

APPENDICES

Appendix A

LabVIEW Block Diagram



Appendix B

Wave tests characteristics
Table 20: Test waves characteristics.

Scale	Wave	s	λ_F	H_F	T_F	λ_M	H_M	T_M	h/λ	$H/(gT^2)$	$h/(gT^2)$
[-]	[-]	[%]	[m]	[m]	[s]	[m]	[m]	[s]	[-]	[-]	[-]
60	Wave 1 a	2.40%	104.17	2.50	8.17	1.74	0.042	1.05	1.27	0.0038	0.202
60	Wave 2 a	2.70%	92.59	2.50	7.70	1.54	0.042	0.99	1.43	0.0043	0.227
60	Wave 3 a	3.00%	83.33	2.50	7.31	1.39	0.042	0.94	1.58	0.0048	0.252
60	Wave 4 a	3.30%	75.76	2.50	6.97	1.26	0.042	0.90	1.74	0.0053	0.277
43.8	Wave 1 b	2.40%	104.17	2.50	8.17	2.38	0.057	1.23	0.93	0.0038	0.147
43.8	Wave 2 b	2.70%	92.59	2.50	7.70	2.11	0.057	1.16	1.04	0.0043	0.166
43.8	Wave 3 b	3.00%	83.33	2.50	7.31	1.90	0.057	1.10	1.16	0.0048	0.184
43.8	Wave 4 b	3.30%	75.76	2.50	6.97	1.73	0.057	1.05	1.27	0.0053	0.202
23.5	Wave 1 c	2.40%	104.17	2.50	8.17	4.43	0.106	1.68	0.50	0.0038	0.079
23.5	Wave 2 c	2.70%	92.59	2.50	7.70	3.94	0.106	1.59	0.56	0.0043	0.089
23.5	Wave 3 c	3.00%	83.33	2.50	7.31	3.55	0.106	1.51	0.62	0.0048	0.099
23.5	Wave 4 c	3.30%	75.76	2.50	6.97	3.22	0.106	1.44	0.68	0.0053	0.109
15.5	Wave 1 d	2.40%	104.17	2.50	8.17	6.72	0.161	2.07	0.33	0.0038	0.052
15.5	Wave 2 d	2.70%	92.59	2.50	7.70	5.97	0.161	1.96	0.37	0.0043	0.059
15.5	Wave 3 d	3.00%	83.33	2.50	7.31	5.38	0.161	1.86	0.41	0.0048	0.065
15.5	Wave 4 d	3.30%	75.76	2.50	6.97	4.89	0.161	1.77	0.45	0.0053	0.072

Appendix C1

Spring readings code

```
1 clc;
2 clear all;
3 close all;
4
5 % Mass with which the spring was tested
6 mass = 0.05;
7
8 % Name of the file with the readings from the current test
9 data_spring = read_data_spring("Test_4.lvm");
10 %read_data_spring is a function created automatically by
    matlab when using the "Import Data" tool to read a .lvm
    file of this format.
11
12 time = data_spring(:, 1);
13 force = data_spring(:, 2);
14
15 dt = time(2) - time(1);
16
17 % Bandpass filter for frequencies between 0.2Hz and 3.5Hz
18 clean_force = bpass2(force, dt, 0.2, 3.5);
19
20 % Identifying peaks from the time series
21 [pks, locs] = findpeaks(clean_force);
22
23 % Assuming there are at least 10 peaks
24 if length(locs) >= 10
25     period = time(locs(10)) - time(locs(9));
26
27     % Calculate the stiffness
28     k = (2 * pi() * (1 / period))^2 * mass; % N/m
29
30     % Check the plot for possible errors.
31     figure()
32     grid on
33     plot(time, clean_force)
```

```
34 else
35     fprintf('%s\n', 'Error: Insufficient peaks for
           stiffness calculation. ');
36 end
```

Matlab codes

Appendix C2

Force computing program

```
1 clear
2 close all
3 clc
4
5 % Input data directory. (Same location as the program)
6 file_path = "";
7
8 % Number of lines.
9 number_lines = 4;
10
11 % Search for all files.
12 filenames = dir(fullfile(file_path, '*.lvm'));
13
14 % Load matrix with intervals for each file
15 load('IntervalsForces.mat');
16 load('f_cut.mat');
17
18 % Number of files.
19 number_files = size(Intervalsforces, 1);
20
21 %% Main loop.
22 for i = 1:35
23     file(i).name = strcat('Test_', Intervalsforces(i, 2),
24         Intervalsforces(i, 1), '_', Intervalsforces(i, 3), '
25         .lvm');
26
27     fprintf('%s%s\n',"Working on: config ",file(i).name);
28
29     % Save name without extension
30
31     file(i).data = get_data_mooring(file(i).name);
32     file(i).inti = str2num(Intervalsforces(i, 4));
33     file(i).inte = str2num(Intervalsforces(i, 5));
```

```

32
33     [file(i).inti(2), file(i).inte(2)] = find_data_inter(
        file(i).data(:, 1), file(i).inti, file(i).inte);
34
35     file(i).time = file(i).data(:, 1);
36     file(i).forces = file(i).data(:, 2:5);
37
38     file(i).dt = file(i).data(2, 1);
39
40     for j = 1:4
41
42         % Clean the signal
43         file(i).forces_clean(:, j) = bpass2(file(i).forces
            (:, j), file(i).dt, 0, f_cut(i));
44         file(i).mean_values(j) = mean(file(i).forces_clean
            (:, j));
45
46         [pks, pklocs] = findpeaks(file(i).forces_clean(
            file(i).inti(2):file(i).inte(2), j), file(i).
            time(file(i).inti(2):file(i).inte(2)));
47         [trs, trlocs] = findpeaks(-file(i).forces_clean(
            file(i).inti(2):file(i).inte(2), j), file(i).
            time(file(i).inti(2):file(i).inte(2)));
48         file(i).peak_data = [pks pklocs; -trs trlocs];
49         [file(i).peak_data(:, 2), I] = sort(file(i).
            peak_data(:, 2));
50         file(i).peak_data(:, 1) = file(i).peak_data(I, 1);
51
52         file(i).amplitude(j, 1) = mean(pks) + mean(trs);
53         for k = 1:length(pklocs) - 1
54             a(k) = pklocs(k + 1) - pklocs(k);
55         end
56         for k = 1:length(trlocs) - 1
57             b(k) = trlocs(k + 1) - trlocs(k);
58         end
59         file(i).period(j, 1) = mean([a b]);
60     end
61
62 end

```

```
63
64 %% Plots
65 for i = 1:28
66
67     figure('units', 'normalized', 'outerposition', [0 0 1
68             1])
69
70     t = tiledlayout(2, 2, 'TileSpacing', 'Compact');
71     title(t, 'Line force time series for wave 1 a', '
72             fontname', 'Times New Roman')
73
74     nexttile
75     plot(file(i).time(file(i).inti(2):file(i).inte(2)),
76           file(i).forces_clean(file(i).inti(2):file(i).inte(2)
77             , 1));
78     title('Time series of load cell n.1', 'fontname', '
79           Times New Roman')
80     legend('Clean force')
81     xlabel('Time[s]')
82     ylabel('Force [N]')
83     grid on
84     hold on
85
86     nexttile
87     plot(file(i).time(file(i).inti(2):file(i).inte(2)),
88           file(i).forces_clean(file(i).inti(2):file(i).inte(2)
89             , 1));
90     title('Time series of load cell n.2', 'fontname', '
91           Times New Roman')
92     legend('Clean force')
93     xlabel('Time[s]')
94     ylabel('Force [N]')
95     grid on
96     hold on
97
98     nexttile
99     plot(file(i).time(file(i).inti(2):file(i).inte(2)),
100          file(i).forces_clean(file(i).inti(2):file(i).inte(2)
101            , 3));
```

```
92     title('Time series of load cell n.3', 'fontname', '
        Times New Roman')
93     legend('Clean force')
94     xlabel('Time[s]')
95     ylabel('Force [N]')
96     grid on
97     hold on
98
99     nexttile
100    plot(file(i).time(file(i).inti(2):file(i).inte(2)),
        file(i).forces_clean(file(i).inti(2):file(i).inte(2)
        , 4));
101    title('Time series of load cell n.4', 'fontname', '
        Times New Roman')
102    legend('Clean force')
103    xlabel('Time[s]')
104    ylabel('Force [N]')
105    grid on
106    hold off
107
108 end
109
110 fprintf('%s \n', 'Program completed!');
```

Appendix C3

Single panel decay tests.

```
1
2 close all;
3 %%
4 clear global;
5 clear all;
6 clc;
7 warning('off', 'all');
8 %%
9 % Output directory for plots.
10 f_out = "../..plots";
11
12 % Input data directory.
13 file_path = "Single_decay/";
14
15 %load parameters.
16 load('Intervals.mat');
17
18 % Number of markers.
19 number_markers = 4;
20
21 % plots off/on [0/1]
22
23 plot_group=0;
24 plot_pkfrequency=1;
25
26 % Load plot colors.
27 colors = colors_matlab();
28
29 % Search for all files.
30 filenames = dir(strcat(file_path, '*.csv'));
31
32 % Number of files.
33 number_files = length(filenames);
34
35 % Tolerance for the "fillmissing" function
```

```
36 tol=0.058;
37
38 % Initializing the export matrices
39 heave_peaks_tot=[0 0 0 0];
40 heave_peaks_a=[0 0 0 0];
41 heave_peaks_b=[0 0 0 0];
42 heave_peaks_c=[0 0 0 0];
43 heave_peaks_d=[0 0 0 0];
44 pitch_peaks_tot=[0 0 0 0];
45 pitch_peaks_a=[0 0 0 0];
46 pitch_peaks_b=[0 0 0 0];
47 pitch_peaks_c=[0 0 0 0];
48 pitch_peaks_d=[0 0 0 0];
49 roll_peaks_tot=[0 0 0 0];
50 roll_peaks_a=[0 0 0 0];
51 roll_peaks_b=[0 0 0 0];
52 roll_peaks_c=[0 0 0 0];
53 roll_peaks_d=[0 0 0 0];
54 %% Start with main loop.
55 for i = 1:number_files
56
57     fprintf('%s%s\n', "Working on: config ", filenames(i).
        name);
58
59     for j=1:size(Intervals,1) % looking for the file in
        the Intervals matrix. If it is not there, it is
        acceptable, but not optimal, and is skipped.
60         flag = 1;
61         if filenames(i).name==Intervals(j,2)
62             flag=0;
63             file(i).inti=str2num(Intervals(j,9));
64             file(i).inte=str2num(Intervals(j,10));
65
66             break
67         end
68     end
69     % I need to end the loop before flagging the structure
        and writing the
70     % message.
```

```
71     if flag==1
72         fprintf('%s%s%s \n','File ',filenames(i).name, '
           was not found in Intervals. It probably has to
           be discarded.')
73         file(i).flag=1;
74         continue
75     else
76         file(i).flag=0;
77     end
78     % done checking the existence of the file.
79
80     %Import data
81     data = import_data(strcat(file_path, filenames(i).name
           ));
82
83     % Save time
84     file(i).time = data(:,1);
85
86     %save name without extension
87     file(i).name=filenames(i).name(1:end-4);
88
89     % check the scale
90
91     switch file(i).name(1:4)
92         case 'roll'
93             switch file(i).name(6)
94                 case 'a'
95                     file(i).scale=60;
96                     file(i).color="#0072BD"; % blue
97                 case 'b'
98                     file(i).scale=43.8;
99                     file(i).color="#D95319"; % orange
100                case 'c'
101                    file(i).scale=23.5;
102                    file(i).color="#EDB120"; % yellow
103                case 'd'
104                    file(i).scale=15.5;
105                    file(i).color="#7E2F8E"; % purple
106            end
```

```

107         otherwise
108             switch file(i).name(7)
109                 case 'a'
110                     file(i).scale=60;
111                     file(i).color="#0072BD";
112                 case 'b'
113                     file(i).scale=43.8;
114                     file(i).color="#D95319";
115                 case 'c'
116                     file(i).scale=23.5;
117                     file(i).color="#EDB120";
118                 case 'd'
119                     file(i).scale=15.5;
120                     file(i).color="#7E2F8E";
121             end
122     end
123
124     % Save position data
125     kk=1;
126     u=zeros(length(data(:,1)),1);
127     for j=1:number_markers
128
129         % Getting the data into the "file" structure
130
131         file(i).marker(j).x = data(:,kk+3);
132         file(i).marker(j).y = data(:,kk+1);
133         [file(i).marker(j).z,TF] = fillmissing(data(:,kk
134             +2),'linear'); %only for heave, the data is
135             filled
136         file(i).marker(j).z=bpass2(file(i).marker(j).z
137             ,1/120,0,10);
138         file(i).TF(j)=sum(TF);
139
140         %Check that the heave data is not too damaged
141
142         if file(i).TF(j)>tol*length(file(i).marker(j).z)
143             fprintf('%s%s%s%s%s%s%s\n',"Heave data on file
144                 ",file(i).name,", marker ", num2str(j), "

```

```
        has over ",num2str(tol*100),"% error");
142     figure()
143     title(strcat("Heave - ", file(i).name, "marker
        ", num2str(j)));
144     subtitle(strcat(" has over ",num2str(tol*100)
        , " % of missing data"));
145     plot(file(i).time,data(:,kk+2));
146 %         return
147     end
148
149     % Getting the initial values
150
151     [i1, i2] = find_data_inter(file(i).time, 0, 1);
152
153     file(i).marker(j).x0 = mean(file(i).marker(j).x(i1
        :i2));
154     file(i).marker(j).y0 = mean(file(i).marker(j).y(i1
        :i2));
155     file(i).marker(j).z0 = mean(file(i).marker(j).z(i1
        :i2));
156     file(i).marker(j).color=colors.(sprintf("%s%s", "
        color_", int2str(j)));
157
158     % getting the ending values
159
160     [I1, I2] = find_data_inter(file(i).time, file(i).
        time(end-60), file(i).time(end-1));
161
162     file(i).marker(j).xf = mean(file(i).marker(j).x(I1
        :I2));
163     file(i).marker(j).yf = mean(file(i).marker(j).y(I1
        :I2));
164     file(i).marker(j).zf = mean(file(i).marker(j).z(I1
        :I2));
165
166     %zeroing the heave data
167
168     file(i).marker(j).z(:)=file(i).marker(j).z(:)-file
        (i).marker(j).zf;
```

```

169
170     % Updating the counter
171
172     kk=kk+3;
173 end
174 % check distances
175 for j=1:number_markers
176     file(i).dist(j)=sqrt((file(i).marker(j).x0-file(i)
177         .marker(1).x0)^2+...
178         (file(i).marker(j).y0-file(i).marker(1).y0)^2)
179         ;
180 end
181 %Here are computed the variables studied. Whether it
182     is heave, roll or pitch
183 [file(i).dist,file(i).I]=sort(file(i).dist);
184
185 switch file(i).name(1:4)
186     case 'heav'
187         for l=1:length(file(i).time)
188             file(i).plot(1)=mean([file(i).marker(1).z(1)
189                 file(i).marker(2).z(1) file(i).marker(3).z(1)
190                 ) file(i).marker(4).z(1)]);
191         end
192     case 'pitc'
193         for l=1:length(file(i).time)
194             file(i).heave_fore(l)=mean([file(i).marker(
195                 file(i).I(1)).z(1) file(i).marker(file(i).I
196                 (2)).z(1)]);
197             file(i).heave_aft(l)=mean([file(i).marker(file
198                 (i).I(3)).z(1) file(i).marker(file(i).I(4)).
199                 z(1)]);
200             file(i).plot(1)=asin((file(i).heave_fore(l)-
201                 file(i).heave_aft(l))/file(i).dist(3))*180/
202                 pi;
203         end
204     case 'roll'
205         for l=1:length(file(i).time)
206             file(i).heave_port(l)=mean([file(i).marker(

```

```

        file(i).I(1)).z(1) file(i).marker(file(i).I
        (3)).z(1)];
197     file(i).heave_starboard(1)=mean([file(i).
        marker(file(i).I(2)).z(1) file(i).marker(
        file(i).I(4)).z(1)]);
198     file(i).plot(1)=asin((file(i).heave_port(1)-
        file(i).heave_starboard(1))/file(i).dist(2))
        *180/pi;
199     end
200 end
201
202 % get the interval with the peaks from the Intervals
        matrix, and
203 % extract the important data from them
204 [I1, I2] = find_data_inter(file(i).time,file(i).inti,
        file(i).inte); % this function finds the indexes
        corresponding to the edges of the interval to be
        studied for the current file.
205 [pks, pklocs] = findpeaks(file(i).plot(I1:I2),file(i).
        time(I1:I2)); % this finds the peaks in said
        interval
206 [trs, trlocs] = findpeaks(-file(i).plot(I1:I2),file(i)
        .time(I1:I2)); % this finds the troughs in said
        interval
207 file(i).peak_data=[pks -trs; pklocs' trlocs']; % this
        puts intervals and troughs together
208 [file(i).peak_data(2,:),I]=sort(file(i).peak_data(2,:)
        );
209 file(i).peak_data(1,:)=file(i).peak_data(1,I); % these
        two lines sort the peaks and troughs
        chronologically
210
211
212 % from the peaks, get simply the amplitude and semi-
        periods
213
214 for j=1:size(file(i).peak_data,2)-1
215     % here, I also transpose it, beware
216     file(i).peaks(j,1)=abs(file(i).peak_data(1,j+1)-

```

```

        file(i).peak_data(1,j));
217     file(i).peaks(j,2)=abs(file(i).peak_data(2,j+1)-
        file(i).peak_data(2,j));
218     end
219
220     % I check that the semi-peaks are decreasing
221     for j=2:size(file(i).peaks,1)
222         if file(i).peaks(j-1,1)<file(i).peaks(j,1)
223             fprintf('%s%s%s \n', 'File ', file(i).name, '
                has non-decreasing half-peaks. Check the
                time series.')
224         end
225     end
226     switch file(i).name(1:4)
227         case 'heav'
228             for j=1:size(file(i).peaks,1)
229                 %Scale-up to full size. They are saved in
                the same matrix
230                 file(i).peaks(j,3)= file(i).peaks(j,1).*
                file(i).scale;
231                 file(i).peaks(j,4)= file(i).peaks(j,2).*
                sqrt(file(i).scale);
232             end
233         otherwise
234             for j=1:size(file(i).peaks,1)
235                 %Scale-up to full size. They are saved in
                the same matrix
236                 file(i).peaks(j,3)= file(i).peaks(j,1);
237                 file(i).peaks(j,4)= file(i).peaks(j,2).*
                sqrt(file(i).scale);
238             end
239     end
240
241     %Record the data into one matrix for each DOF to
    export
242     switch file(i).name(1:4)
243         case 'heav'
244             heave_peaks_tot=[heave_peaks_tot;file(i).peaks
                ];

```

```
245         switch file(i).scale
246             case 60
247                 heave_peaks_a=[heave_peaks_a;file(i).
                peaks];
248             case 43.8
249                 heave_peaks_b=[heave_peaks_b;file(i).
                peaks];
250             case 23.5
251                 heave_peaks_c=[heave_peaks_c;file(i).
                peaks];
252             case 15.5
253                 heave_peaks_d=[heave_peaks_d;file(i).
                peaks];
254         end
255     case 'pitc'
256         pitch_peaks_tot=[pitch_peaks_tot;file(i).peaks
        ];
257         switch file(i).scale
258             case 60
259                 pitch_peaks_a=[pitch_peaks_a;file(i).
                peaks];
260             case 43.8
261                 pitch_peaks_b=[pitch_peaks_b;file(i).
                peaks];
262             case 23.5
263                 pitch_peaks_c=[pitch_peaks_c;file(i).
                peaks];
264             case 15.5
265                 pitch_peaks_d=[pitch_peaks_d;file(i).
                peaks];
266         end
267     case 'roll'
268         roll_peaks_tot=[roll_peaks_tot;file(i).peaks];
269         switch file(i).scale
270             case 60
271                 roll_peaks_a=[roll_peaks_a;file(i).
                peaks];
272             case 43.8
273                 roll_peaks_b=[roll_peaks_b;file(i).
```

```

                peaks];
274         case 23.5
275             roll_peaks_c=[roll_peaks_c;file(i).
                peaks];
276         case 15.5
277             roll_peaks_d=[roll_peaks_d;file(i).
                peaks];
278         end
279     end
280 end
281 %%
282 for ii=[1:9 11 13 17 19 20 23:26 28:30 32:37 43 44 46:50
        52 54:56 59:68 70:76]
283
284     d = log(file(ii).peaks(1,3)/file(ii).peaks(2,3));
285     file(ii).damp1 = d/sqrt(4*pi^2+d^2);
286     file(ii).natfr = 2*pi/(file(ii).peaks(1,4)*sqrt(1-file
        (ii).damp1^2));
287 end
288
289 %% plot individual
290 heave_peaks_tot(1,:)=mean(heave_peaks_tot(2:end,:),1);
291 heave_peaks_a(1,:)=mean(heave_peaks_a(2:end,:),1);
292 heave_peaks_b(1,:)=mean(heave_peaks_b(2:end,:),1);
293 heave_peaks_c(1,:)=mean(heave_peaks_c(2:end,:),1);
294 heave_peaks_d(1,:)=mean(heave_peaks_d(2:end,:),1);
295
296 pitch_peaks_tot(1,:)=mean(pitch_peaks_tot(2:end,:),1);
297 pitch_peaks_a(1,:)=mean(pitch_peaks_a(2:end,:),1);
298 pitch_peaks_b(1,:)=mean(pitch_peaks_b(2:end,:),1);
299 pitch_peaks_c(1,:)=mean(pitch_peaks_c(2:end,:),1);
300 pitch_peaks_d(1,:)=mean(pitch_peaks_d(2:end,:),1);
301
302 roll_peaks_tot(1,:)=mean(roll_peaks_tot(2:end,:),1);
303 roll_peaks_a(1,:)=mean(roll_peaks_a(2:end,:),1);
304 roll_peaks_b(1,:)=mean(roll_peaks_b(2:end,:),1);
305 roll_peaks_c(1,:)=mean(roll_peaks_c(2:end,:),1);
306 roll_peaks_d(1,:)=mean(roll_peaks_d(2:end,:),1);
307

```

```
308 figure(4)
309 hold on
310 grid on
311 title("Heave", 'FontSize',16)
312 xlabel('Period [s]', 'FontSize',16);
313 ylabel('Heave [m]', 'FontSize',16);
314
315 scatter (heave_peaks_a(1,4),heave_peaks_a(1,3), '
    MarkerFaceColor', "#0072BD", 'MarkerEdgeColor', 'k')
316 scatter (heave_peaks_b(1,4),heave_peaks_b(1,3), '
    MarkerFaceColor', "#D95319", 'MarkerEdgeColor', 'k')
317 scatter (heave_peaks_c(1,4),heave_peaks_c(1,3), '
    MarkerFaceColor', "#EDB120", 'MarkerEdgeColor', 'k')
318 scatter (heave_peaks_d(1,4),heave_peaks_d(1,3), '
    MarkerFaceColor', "#7E2F8E", 'MarkerEdgeColor', 'k')
319
320 legend('60 scale', '43.8 scale', '23.5 scale', '15.5 scale')
321
322 figure(5)
323 hold on
324 grid on
325 title("Pitch", 'FontSize',16)
326 xlabel('Period [s]', 'FontSize',16);
327 ylabel('Pitch [ ]', 'FontSize',16);
328
329 scatter (pitch_peaks_a(1,4),pitch_peaks_a(1,3), '
    MarkerFaceColor', "#0072BD", 'MarkerEdgeColor', 'k')
330 scatter (pitch_peaks_b(1,4),pitch_peaks_b(1,3), '
    MarkerFaceColor', "#D95319", 'MarkerEdgeColor', 'k')
331 scatter (pitch_peaks_c(1,4),pitch_peaks_c(1,3), '
    MarkerFaceColor', "#EDB120", 'MarkerEdgeColor', 'k')
332 scatter (pitch_peaks_d(1,4),pitch_peaks_d(1,3), '
    MarkerFaceColor', "#7E2F8E", 'MarkerEdgeColor', 'k')
333
334 legend('60 scale', '43.8 scale', '23.5 scale', '15.5 scale')
335
336 figure(6)
337 hold on
338 grid on
```

```
339 title("Roll", 'FontSize',16)
340 xlabel('Period [s]', 'FontSize',16);
341 ylabel('Roll [ ]', 'FontSize',16);
342
343 scatter (roll_peaks_a(1,4),roll_peaks_a(1,3), '
    MarkerFaceColor', "#0072BD", 'MarkerEdgeColor', 'k')
344 scatter (roll_peaks_b(1,4),roll_peaks_b(1,3), '
    MarkerFaceColor', "#D95319", 'MarkerEdgeColor', 'k')
345 scatter (roll_peaks_c(1,4),roll_peaks_c(1,3), '
    MarkerFaceColor', "#EDB120", 'MarkerEdgeColor', 'k')
346 scatter (roll_peaks_d(1,4),roll_peaks_d(1,3), '
    MarkerFaceColor', "#7E2F8E", 'MarkerEdgeColor', 'k')
347
348 legend('60 scale', '43.8 scale', '23.5 scale', '15.5 scale')
349
350 %% plots. full scale, amplitude vs frequency
351
352 if plot_pkfrequency==1
353     figure(1)
354     hold on
355     grid on
356     title("Heave", 'FontSize',16)
357     xlabel('Period [s]', 'FontSize',16);
358     ylabel('Heave [m]', 'FontSize',16);
359
360     figure(2)
361     hold on
362     grid on
363     title("Pitch", 'FontSize',16)
364     xlabel('Period [s]', 'FontSize',16);
365     ylabel('Pitch [ ]', 'FontSize',16);
366
367     figure(3)
368     title("Roll", 'FontSize',16)
369     xlabel('Period [s]', 'FontSize',16);
370     ylabel('Roll [ ]', 'FontSize',16);
371     grid on
372     hold on
373
```



```
374     for i=1:number_files
375         if file(i).flag==1
376             continue
377         end
378         switch file(i).name(1:4)
379             case 'heav'
380                 figure(1)
381                 hold on
382                 scatter(file(i).peaks(:,4),file(i).peaks
383                     (:,3),'MarkerFaceColor',file(i).color,'
384                         MarkerEdgeColor','k');
385             case 'pitc'
386                 figure(2)
387                 hold on
388                 scatter(file(i).peaks(:,4),file(i).peaks
389                     (:,3),'MarkerFaceColor',file(i).color,'
390                         MarkerEdgeColor','k');
391             case 'roll'
392                 figure(3)
393                 hold on
394                 scatter(file(i).peaks(:,4),file(i).peaks
395                     (:,3),'MarkerFaceColor',file(i).color,'
396                         MarkerEdgeColor','k');
397         end
398     end
399 end
400 fprintf('%s \n', 'Program completed!');
401
402
403 %% Plot time series of studied degree of freedom for each
404 test.
405 if plot_group==number_files
406     for i=76
407         if file(i).flag==1
408             continue
409         end
410         figure('units','normalized','outerposition',[0 0 1
411             1])
412         hold on; grid on;
```

```
405     switch file(i).name(1:4)
406     case 'heav'
407         title(strcat("Heave - ", file(i).name))
408         xlabel('Time [s]');
409         ylabel('Heave [m]');
410     case 'pitc'
411         title(strcat("Pitch - ", file(i).name))
412         xlabel('Time [s]');
413         ylabel('Pitch [ ]');
414     case 'roll'
415         title(strcat("Roll - ", file(i).name))
416         xlabel('Time [s]');
417         ylabel('Roll [ ]');
418     end
419
420     plot(file(i).time,file(i).plot,'LineWidth',1);
421     legend('Mean of the bypassed');
422 end
423 end
```

Matlab codes

Appendix C4

Bandpass filter

```
1 function [xbp] = bpass2(x,dt,flow,fhigh)
2 %
   -----
3 % Matlab function that will band pass filter time series
   in matrix x
4 %
5 % I    x(1:nsamples,1:ntimeseries)= timeseries matrix
6 % I    dt = time step (s)
7 % I    flow and fhigh = lower and upper cut-off
   frequencies [Hz]
8 % O    xbp = band passed filtered time series
9 %
10 % H. Lie, Marintek, 09.04.2002 & T. Kristiansen, Marintek,
   12.02.2004
11 % S. Saettone, DTU & NTNU, 08.10.2018
12 %
   -----
13
14 nsamples = length(x(:,1));
15 N=nsamples;
16 domega = 2*pi/(dt*nsamples);
17 df=domega/(2*pi);
18 nlow=floor(flow/df);
19 nhigh=ceil(fhigh/df);
20
21 if even(nsamples)
22     nh = nsamples/2;
23     ivec1=1:nlow;
24     ivec2=nhigh:nh;
25     ivec3=(nh+1):(N-nhigh+1);
26     ivec4=(N-nlow+1):N;
```

```
27 else
28     nh = (nsamples-1)/2;
29     ivec1=1:nlow;
30     ivec2=nhigh:nh;
31     ivec3=(nh+1):(N-nhigh+1);
32     ivec4=(N-nlow+1):N;
33 end
34
35 Fx = fft(x);
36
37 %---- Band-pass filter signals ----
38
39 % Gaussian window.
40 beta = 0.005;
41 alpha=log(3)/(flow*beta);
42 gamma=log(3)/(fhigh*beta);
43
44 fvec1=ivec1*df;
45 fvec2=ivec2*df;
46 fvec3=ivec3*df;
47 fvec4=ivec4*df;
48
49 window1=exp(-(alpha*(fvec1-flow).^2));
50 window2=exp(-(gamma*(fvec2-fhigh).^2));
51 window3=exp(-(gamma*(fvec3-(N-nhigh+1)*df).^2));
52 window4=exp(-(alpha*(fvec4-(N-nlow+1)*df).^2));
53
54 Fx(ivec1)=Fx(ivec1).*window1';
55 Fx(ivec2)=Fx(ivec2).*window2';
56 Fx(ivec3)=Fx(ivec3).*window3';
57 Fx(ivec4)=Fx(ivec4).*window4';
58
59 % Transform back to time domain.
60 xbp = real(ifft(Fx));
61
62 end
```
